Electron localization in water clusters. II. Surface and internal states

R. N. Barnett, Uzi Landman, and C. L. Cleveland
School of Physics, Georgia Institute of Technology, Atlanta, Georgia 30332

Joshua Jortner
School of Chemistry, Tel Aviv University, 69978, Tel Aviv, Israel

(Received 5 November 1987; accepted 8 December 1987)

Electron attachment and localization in small water clusters $(H_2O)_n$ ($n = 8$–128) is studied using path-integral molecular dynamics simulations. The electron-water molecule interaction is described via a pseudopotential which includes Coulomb, polarization, exclusion and exchange contributions. Different electron localization modes are found depending on cluster size. For small and intermediate size clusters ($n = 8$–32), the energetically favored localization mode involves a surface state and the calculated excess electron binding energies are in agreement with experimentally measured values. In larger clusters, $n = 64$, 128, internal localization (solvation) is energetically favored. In both cases the localization of the excess electron is accompanied by large cluster molecular reorganization. The cluster size dependence of the localization mode, the energetics, structure, and excess electron distributions in the negative molecular anions $(H_2O)_n^-$, and the dependence on temperature are explored.

I. INTRODUCTION

The mechanisms and energetics of electron solvation in fluids have been the subject of extensive theoretical and experimental efforts since the discovery of electron solvation in liquid ammonia in 1863[1] and of the generation of "hydrated electrons" via pulse radiolysis of liquid water in 1962.[2] On the theoretical side, various models of solvation phenomena have been proposed and implemented.[3–6] These studies employed various theoretical methods and model interactions yielding information of varied degrees of refinement and microscopic detail. These models include dielectric continuum approaches[7,8] in which the discrete molecular nature is neglected, semicontinuum studies[9–14] where a discrete cluster of a prescribed structure is embedded in a dielectric continuum, statistical mechanical models employing model fluids and path-integral functional methods,[15] path-integral simulations[16–29] using interaction potentials of various degrees of microscopic complexity, and cluster quantum-chemical all-electron calculations[13,14,30] in which the energetics is investigated for a finite set of cluster configurations. The key issues in these studies are the nature of interactions, the response of the fluid, the dynamics and mechanisms of localization and solvation, and the elucidation of optical spectroscopic data which in the case of excess electrons in polar solvents is characterized by structureless, broad absorption spectra, asymmetric toward the band maximum. In the case of the hydrated electron, the band maximum is at 1.73 eV at atmospheric pressures,[31] and is pressure dependent, shifting to 2.0 eV when the pressure is increased to 6.3 kbar.[32] In addition, analysis of electron spin resonance (ESR) measurements on trapped electrons in γ-irradiated alkaline glass and ^{17}O enriched alkaline ice glasses[33,34] indicate that the electron is surrounded by six water molecules with their oxygens forming an octahedral cage, and that the OH bond of the six water molecules are oriented toward the electron, in contrast to some previous models[9–14,30] which assumed that in the energetically favorable configuration the molecular dipoles are oriented toward the trapped electron. It is however, not clear whether these alkaline glass systems provide a realistic representation of electron solvation in liquid water.

The recent discovery of electron attachment to small water and ammonia clusters[35–41] opens new avenues for microscopic studies of electron localization and solvation. In particular, by varying the cluster size, it is possible to explore the transition from the molecular to the condensed phase regimes, and the size effect on structural, dynamical, quantum, and chemical aspects of the problem. Furthermore, the finite size of these systems and the large surface to volume ratio gives rise to the manifestation of surface phenomena.

Electron attachment to molecular clusters allows theoretical and experimental interrogation of the energetics and dynamics of electron localization and of the following physical and chemical phenomena:

(1) The parentage problem. In many interesting cases the excess electron is attached to a cluster whose individual atomic or molecular constituents do not form a stable negative ion.

(2) Localized and extended states of the excess electron. The spatial extent of the electron charge distribution, i.e., the localization length, relative to the cluster size, provides a distinction between localized and extended states in a finite system.

(3) Bulk and surface states of the excess electron. The relative energetic stability of these two distinct types of states in different clusters is of considerable interest.

(4) Cluster reorganization. The energetically stable state of the electron attached to the cluster may involve a nuclear reorganization, and electron attachment is accompanied by a large cluster reorganization energy.

(5) Cluster isomerization induced by electron attachment.[28] Related to the cluster reorganization mentioned above the attachment of an electron to a cluster may result in a configurational change resulting in a close-energy isomer. This phenomena exhibits itself in the sequence of structural transformations (isomerizations) which the negatively

 0021-9606/88/074429-19$02.10

charged cluster undergoes as the temperature is increased.

With regard to the parentage issue, it is established that a single water or ammonia molecule does not readily localize an excess electron without a major configurational distortion.[42–44] Such intramolecular distortion amounts to the formation of a new chemical species, e.g., the formation of weakly bound $H_2 + O^-$ or $H + OH^-$ accompanying electron attachment to a water molecule. The wealth of experimental information pertaining to the optical, magnetic, and transport properties of metal–ammonia solutions and of the hydrated electron in water[1–6,31,45–52] and of the trapped electron in ice[33,52] precludes the notion of large intramolecular distortions. Accordingly, electron localization in these and other polar fluids is nonreactive, involving cooperative solvation which originates from the combination of long-range and short-range interactions and which is accompanied by large local solvent reorganization. In this context, studies of microscopic solvation effects of an excess electron in well characterized environments would allow for the separation of the role of the short-range forces and of the long-range attractive interactions in electron solvation.

The issue of electron localization modes, i.e., surface versus bulk (interior) states, is manifested by the ubiquity of surface states of excess electrons on clusters which were predicted for vacancy-free alkali–halide clusters[53] and for helium clusters.[54] This raises the distinct possibility, which is indeed verified, that such surface states play an important role in electron localization on water clusters.

Finally, the phenomenon of nonreactive electron attachment to molecular clusters raises the issue of the size effect on chemical and physical phenomena,[55,56] in particular, that of the minimal size of a (water or ammonia) cluster which sustains a bound state of the excess electron and the temperature dependence of the process.

Early information on electron attachment to clusters of polar molecules emerged from studies of the absorption spectra of excess electrons in supercritical ammonia and water.[52,57,58] A dramatic difference between the characteristic density for electron localization in D_2O and ND_3 was tentatively attributed[57,59] to the larger size of the (preexisting) clusters of ammonia, as compared to those of water, which are required for electron attachment. Unfortunately, the information emerging from such bulk experiments is intrinsically limited, as the size of the preexisting cluster and the final cluster attaching the excess electron can only be inferred indirectly. As is often the case, progress in this field has been made possible by new experimental techniques being used in an imaginative fashion. The advent of supersonic and cluster beams allowed for the experimental investigation of the size effects and the energetics of the electron attachment to water and ammonia clusters. Through these experiments, the following information became available:

(1) The water dimer constitutes the smallest water cluster which attaches an electron,[37,38] resulting in a weakly bound $(H_2O)_2^-$ state, with an estimated binding energy of ~ 17 meV. We note the high degree of uncertainty of this value due to the nature of the experiment (field detachment) and various assumptions introduced in the course of analysis of the results.

(2) Strongly bound $(H_2O)_n^-$ clusters are observed[35–41] for $n > 11$. This critical cluster size does not depend on the isotopic composition of the water molecules.

(3) The stable $(H_2O)_n^-$ ($n > 11$) clusters are characterized[39] by a large electron vertical binding energy (EVBE) which varies from EVBE $= -0.75$ eV for $n = 11$ to EVBE $= -1.12$ eV for $n = 19$.

(4) Nonreactive localization in water clusters was experimentally documented to originate either from electron binding during the cluster nucleation process[35–39] or by electron attachment to preexisting clusters.[40,41]

(5) A striking difference is exhibited between the minimum cluster size for the formation of $(H_2O)_n^-$ ($n \geqslant 11$) and of $(NH_3)_n$ ($n \geqslant 35$).[36,37]

The occurrence of a weakly bound state in $(H_2O)_2^-$ [observation (1)] can be understood on the basis of quantum path integral molecular dynamics calculation to originate from long-range electron–dipole interaction.[22,28] Quantum-chemical calculations[60] and path-integral simulations[22,28] predict electron binding in a diffuse state with an equilibrium average vertical electron binding energy of -3 meV and an electron distribution whose radius of gyration is $\sim 36\, a_0$, at 20 K. The equilibrium averaged nuclear configuration of the water molecules in $(H_2O)_2^-$ is similar to that of the neutral, $(H_2O)_2$ cluster. Detailed examination of the path-integral simulation[28] results and recent studies of the real time evolution of the system,[61] using a method which combines the classical molecular dynamics of the water molecules with a self-consistent solution of the time-dependent Schrödinger equation for the electron, reveal that the $(H_2O)_2^-$ cluster is highly fluctional. Accordingly, the nuclear configuration oscillates between the above mentioned low dipole moment configuration, $\sim 1\, ea_0 = 2.524$ D, and nuclear configurations in which the total dipole moment of the water dimer is as large as $1.5\, ea_0$. These fluctuations are accompanied by fluctuations in the excess electron vertical binding energy[28,61] between the above mentioned value of -3 meV for the low-dipole moment configuration, and a value as high as -24 meV, corresponding to a high dipole moment configuration (note the experimental estimate of -17 meV).

On the other hand, the experimental observation of stable $(H_2O)_n^-$ ($n \geqslant 11$) clusters [observations (2)–(5)] poses a challenging theoretical problem, as the origin of the energetic stability of the excess electron clusters is not clear. Self-consistent-field-configuration-interaction calculations in conjunction with estimates of the water–water interactions were conducted for $(H_2O)_n^-$ ($n = 6,8$) clusters.[30,62] These quantum mechanical calculations reveal that the electron adiabatic binding energy (EABE), which corresponds to the energetic change in the process $(H_2O)_n^{(eq)} + e \rightarrow (H_2O)_n^-$ is positive for $(H_2O)_6^-$, $(H_2O)_8^-$ and also presumably for larger water clusters. This result precludes the existence of such excess electron clusters, in contrast with experiment. These theoretical studies followed faithfully the conventional wisdom in the field of solvated electron theory, invoking the implicit assumption that the excess electron state in $(H_2O)_n^-$ constitutes an internal localization mode.

The quantum path integral molecular dynamics

(QUPID) method[16–29] is ideally suited to explore the localization modes of an excess electron in water clusters, which is the subject matter of the present paper. We report on a QUPID study of electron attachment to $(H_2O)_n$ clusters over a broad range of cluster sizes ($n = 8$–128) and over a wide temperature domain ($T = 79$–300 K). From the technical point of view we have advanced a new electron–water pseudopotential in the spirit of the density functional theory, providing a general approach to the exploration of the interaction of an excess electron with a variety of polar molecules (see paper I[63]). From the point of view of general methodology two major conclusions emerge from our study. First, electron localization in medium-sized ($8 \leqslant n < 32$) water clusters does not involve the precursor of the celebrated solvated electron, but rather constitutes a novel excess electron surface state on a water cluster. Preliminary reports of these results were already presented.[28,29] Secondly, upon increasing the size of the water clusters the internal electron localization mode becomes energetically favored. The "transition" from surface to internal electron localization mode occurs in the range of cluster sizes $32 < n < 64$, providing the signature of the onset of a substantial contribution from long-range attractive interactions to excess electron localization in large water clusters.

In Sec. II we outline the quantum path-integral molecular dynamics method which we used in our study, and the interaction potentials which were described in detail in the preceding paper[63] (referred to as paper I). Our results are given in Sec. III.

II. QUANTUM PATH INTEGRAL MOLECULAR DYNAMICS AND INTERACTION POTENTIALS

The quantum path–integral molecular dynamics method (QUPID) rests on an isomorphism between the Feynman path-integral formulation of quantum statistical mechanics[64] and a classical problem wherein the quantum particle(s) is represented by a cyclic necklace of P pseudoparticles ("beads"), where P is the number of points on the discretized path.[65] Each point on the path interacts with its nearest neighbor via a harmonic potential and with any external potential (e.g., interactions with another quantum particle or with classical degrees of freedom) via the interaction potential reduced by the factor P^{-1}. The isomorphism is exact in the limit $P \to \infty$, and the choice of P in implementations of the method depends on the temperature and nature of interactions. As a rule of thumb, for an electron interacting with water molecules, we found[29] that adequate discretization is achieved for $P k_B T \geqslant e^2/a_0$ where k_B is Boltzmann's constant, T is the temperature, e is the electron charge and a_0 is the Bohr radius. In the classical isomorphism the quantum-mechanical averages are replaced by averages over the phase-space generated by an effective classical Hamiltonian which is derived via the path-integral formulation of the quantum partition function. These averages can be evaluated by a Monte Carlo calculation or, as we apply in our study, as averages over the phase-space trajectories obtained via integration of the classical equations of motion generated by the effective Hamiltonian.[16] As such, the only physical information which these simulations yield pertains to the equilibrium (energetic and structural) properties and no direct real time dynamical data[61] is obtained by this method.

For a system of N water molecules with $\{\mathbf{R}_{i\alpha}\}$ denoting collectively the coordinates of the nuclei ($i = 1$–3 corresponding to one oxygen and two hydrogens) in the αth water molecule ($\alpha = 1,\ldots,N$), and $\mathbf{r}_j$ denoting the coordinate of the jth bead, the total Hamiltonian for the isomorphic classical system is given by

$$H = \frac{1}{2}\sum_{\alpha=1}^{N}\sum_{i=1}^{3} m_i \dot{\mathbf{R}}_{i\alpha}^2 + \sum_{\alpha=1}^{N}\left[\phi^{(1)}(\{\mathbf{R}_{i\alpha}\}) + \frac{1}{2}{\sum_{\alpha,\alpha'}}'\phi^{(2)}(\{\mathbf{R}_{i\alpha}\},\{\mathbf{R}_{j\alpha'}\})\right] + \frac{P m_e}{2\beta\hbar^2}\sum_{i=1}^{P}(\mathbf{r}_i - \mathbf{r}_{i+1})^2 + \frac{1}{P}\sum_{\alpha=1}^{N}\sum_{j=1}^{P} V(\mathbf{r}_j,\{\mathbf{R}_{i\alpha}\}) + \frac{1}{2}\sum_{i=1}^{P} m^* \dot{\mathbf{r}}_i^2, \quad (1)$$

where m_e is the mass of the electron, $\beta = 1/k_B T$, and m_i and m^* are the dynamic masses of the oxygen and hydrogen and of the electron (m^*) which are arbitrary (since the equilibrium averages generated by the Hamiltonian in Eq. (1) are independent of the masses). In our calculations the dynamic masses of the atoms were taken as the proton mass, and to maximize computational efficiency m^* was taken in the range of 0.025 to 0.1 of the proton mass, with the lower value at low temperature. The integration time step Δt which we used is 0.25 t.u., where the time unit t.u. $= 1.054 \times 10^{-15}$ s. Our molecular dynamics simulations are performed at constant temperature (canonical ensemble) with the velocity form of the Verlet integration algorithm.[66]

The first and last terms in Eq. (1) are kinetic terms. $\phi^{(1)}$ and $\phi^{(2)}$ are the intras and intermolecular potentials of the water molecules which are modeled via the RWK2-M model[67] (see paper I, Sec. III) and V is the electron–water molecule interaction potential (see Sec. II of paper I).

Invoking previous formalism and notation[28,29] the average total energy of the system is

$$E = \frac{3(3N)}{2\beta} + \langle \Phi^{(1)} + \Phi^{(2)} \rangle + K + \langle V \rangle, \quad (2)$$

where

$$K = \frac{3}{2\beta} + \frac{1}{2P}\sum_{\alpha=1}^{N}\sum_{j=1}^{P}\left\langle \frac{\partial V(\mathbf{r}_j,\{\mathbf{R}_{i\alpha}\})}{\partial \mathbf{r}_j}\cdot(\mathbf{r}_j - \mathbf{r}_P)\right\rangle, \quad (3a)$$

and

$$\langle V \rangle = \left\langle \frac{1}{P}\sum_{\alpha=1}^{N}\sum_{j=1}^{P} V(\mathbf{r}_j,\{\mathbf{R}_{i\alpha}\})\right\rangle. \quad (3b)$$

The angular brackets indicate statistical equilibrium averages over particle trajectories generated via integration of the equations of motion corresponding to the Hamiltonian given in Eq. (1). $\Phi^{(1)}$ and $\Phi^{(2)}$ are the total intra and intermolecular interaction energies respectively [second and third terms on the right-hand side of Eq. (1)].

In Eq. (2) the first term is the kinetic energy of the $3N$ classical degrees of freedom. The second term is the equilibrium average of the inter and intra atomic interaction with

the water molecules. The third term [Eq. (3a)] is separated into the kinetic energy of a free particle ($3/2\beta$) and the interaction kinetic energy,[16,68] $K_{\rm int}$ [second term on the right-hand side in Eq. (3a)].

The energetics of the systems which we study is expressed in terms of the electron vertical binding energy (EVBE) electron adiabatic binding energy (EABE) and cluster reorganization energy (E_c),

$$\text{EVBE} = K_{\rm int} + \langle V \rangle, \tag{4}$$

$$\text{EABE} = \text{EVBE} + E_c, \tag{5}$$

$$E_c = \langle \Phi^{(1)} + \Phi^{(2)} \rangle_{(\mathrm{H_2O})_n^-} - \langle \Phi^{(1)} + \Phi^{(2)} \rangle_{(\mathrm{H_2O})_n}. \tag{6}$$

The cluster reorganization energy [Eq. (6)] is the difference between the equilibrium intramolecular and intermolecular potential energies in the negatively charged $[(\mathrm{H_2O})_n^-]$ and the corresponding equilibrium neutral $[(\mathrm{H_2O})_n]$ clusters. EVBE is the energy required to detach the electron from the $(\mathrm{H_2O})_n^-$ cluster without allowing nuclear rearrangement to occur and is the quantity measured in photoelectron spectroscopy.[39] The energetic stability of the negatively charged cluster with respect to the equilibrium neutral cluster plus free electron is inferred from the magnitude and sign of EABE (negative value corresponding to a stable bound state). Note that these definitions differ in sign from those of the corresponding electron affinities used in our earlier publication.[29]

A characterization of the extent of the bead distribution for the excess electron is given by the radius of gyration R_g,

$$R_g^2 = \frac{1}{2P^2} \left\langle \sum_{i,j} (\mathbf{r}_i - \mathbf{r}_j)^2 \right\rangle, \tag{7}$$

and the degree of localization by the complex time-correlation function[15] $\mathscr{R}(t-t')$,

$$\mathscr{R}^2(t-t') = \langle |\mathbf{r}(t) - \mathbf{r}(t')|^2 \rangle, \quad t - t' \epsilon (0, \beta\hbar), \tag{8}$$

where $\mathbf{r}(t)$ is the position along the electron path at time t (location of a bead on the necklace in the classical isomorphism). From Eq. (8), the correlation length is defined as the value at $t - t' = \beta\hbar/2$, i.e., $\mathscr{R}(\beta\hbar/2)$ is the diameter of the necklace which for a free particle is denoted by $\mathscr{R}_f = \sqrt{3}\lambda_T/2$, where λ_T is the thermal wavelength of the electron, i.e., $\lambda_T = (\hbar^2/\beta m_e)^{1/2} \approx 32.45\ a_0$, at room temperature. Further discussion of $\mathscr{R}^2(t-t')$ and its use in estimating[15] excitation energies are given in the next section.

An additional quantity which has been used[19] for characterization of the spatial extent of the quantum particle is R_T defined by

$$R_T \equiv \left[\frac{P}{P-1} \sum_{i=1}^{P} \langle (\mathbf{r}_i - \mathbf{r}_{i+1})^2 \rangle \right]^{1/2}, \tag{9}$$

which for a free particle takes the value $R_T^f = \sqrt{3}\lambda_T$, (i.e., $R_T^f = 2\mathscr{R}_f$). Additionally, it is of interest to note the relation $(1/2)\mathrm{R_T} = \sqrt{P}\,\mathscr{R}(\beta\hbar/\mathrm{P})$.

In our simulations we have employed the electron–water molecule pseudopotential which we have constructed and discussed in detail in paper I.[63] This potential consists of Coulomb ($V_{\rm Coul}$), polarization (V_p), exclusion (V_e), and exchange (V_x) contributions,

$$V(\mathbf{r},\mathbf{R}_0,\mathbf{R}_1,\mathbf{R}_2) = V_{\rm Coul} + V_p + V_e + V_x, \tag{10}$$

where $\mathbf{r}$ is the electron coordinate, and $\mathbf{R}_0$, $\mathbf{R}_1$, and $\mathbf{R}_2$ are the coordinates of the oxygen and two hydrogens of the water molecule, respectively.

The intra- and intermolecular interactions in water were described using the RWK2-M potentials[67] which are also given in paper I.[63]

III. ELECTRON LOCALIZATION IN WATER CLUSTERS

Equipped with the simulation method (QUPID) and the interaction potentials described in the previous section (see also paper I), we have embarked upon an investigation of the energetics and structure of $(\mathrm{H_2O})_n^-$ clusters for $n = 8$–128.

A. Preparation

As discussed in Sec. I, the experimental preparation of $(\mathrm{H_2O})_n^-$ clusters can be achieved by electron binding during the cluster nucleation process[35–39] or by electron attachment to a preexisting cluster.[40,41] In correspondence with the alternative experimental methods, and since we discovered different modes of electron localization, i.e., surface vs internal localization, we describe first the methods of preparation employed in our simulations. These preparation methods were developed as a result of extensive experimentation and prove to be most efficient computationally.

1. Surface states

To prepare a surface state we start from an equilibrated neutral cluster of n water molecules at the desired temperature[66] (see below). First we place a necklace containing 2^8 beads which are distributed according to a Gaussian distribution with a width of $2.5\ a_0$. The center of the distribution is located $\sim 2\ a_0$ from the outermost water molecule of the cluster. The system is allowed to evolve at the desired temperature until the radius of gyration of the bead distribution does not vary significantly. At this stage the number of beads is increased to the number P appropriate for the desired temperature and the system is allowed to evolve till equilibrium is achieved, at which time the run continues and statistical averages are collected. We should mention at this stage that for the smaller clusters (8, 12, and 18) several attempts to prepare surface states in this manner resulted in a very diffuse surface state of low binding energy, which were discarded.

2. Internal states

The first stage in preparing an internal state (for $n = 32$, 64, and 128) consists of a condensation of the n molecules around a "classical" electron. The whole system is contained inside a closed cavity of a radius of $35\ a_0$ to assure that molecules will not escape in this preparatory stage. The system evolves classically at constant temperature $T = 400$ K until equilibrium is achieved (small fluctuations in the energy around a mean value). At this point the classical charge is replaced by a necklace of 2^8 beads distributed according to a

Gaussian of width 2.5 a_0, centered about the former classical electron, and the system is allowed to equilibrate at $T = 365$ K, after which the number of beads is increased to 2^{10} and the system evolves for another 5000 Δt. Subsequently the temperature is brought to 300 K (by incrementally reducing the mean of the Maxwellian velocity distribution used in the stochastic collision frequency algorithm used for constant temperature control) over 2000 Δt, the system is allowed to equilibrate and afterwards data is recorded and averaged. For $n = 18$, the same procedure is followed but when the number of beads is increased from 2^8 to 2^{10} the system is cooled down to 158 K (the $n = 18$ cluster does not localize the electron internally at 300 K. Upon heating the low temperature internal state for this cluster to 300 K, it converts to a surface state). We found that adding a small repulsive interaction of the form $\epsilon(\sigma/r)$,^{12} with $\sigma = 5\ a_0$ and $\epsilon = 0.01$ hartree between the classical electron and the oxygens of the water molecules enhances the formation of the cavity around the classical electron and speeds up the calculation, yielding the same final answers.

3. Neutral clusters

In preparing neutral water clusters we start with n randomly distributed water molecules inside a sphere of radius $35\ a_0$. The system is equilibrated at $T = 365$ K using classical molecular dynamics with the RWK2-M interaction potentials (see Sec. III of paper I) and an integration time step of 0.25 t.u. Subsequently the temperature is incrementally ramped down (over 2500 Δt) to 300 K and the simulation continues till equilibrium at this temperature is achieved. In order to obtain low temperature neutral clusters, 25 configurations are selected from the $T = 300$ K equilibrium ensemble and each is cooled down over 2500 Δt to 158 K where the cluster is essentially frozen. We found that when equilibrated at that temperature the dispersion in the energy per molecule between the 25 randomly selected configurations is rather small. The resulting one with the lowest energy is selected. To achieve a lower temperature cluster, that selected configuration is cooled to the desired temperature and equilibrated. The total energies, intra- and interpotential energies and dipole moments for the various neutral cluster sizes at several temperatures are given in Table I. From this table we observe that the aggregation of the water molecules to form a cluster causes structural distortions of the water molecules which are reflected in the values of the equilibrium average intramolecular potential energy $\langle\Phi^{(1)}\rangle$ of the molecules in the cluster [the value of $\langle\Phi^{(1)}\rangle = 0$ for an isolated water molecule is taken as a reference]. A fraction of this value is due to thermal fluctuations which, assuming harmonic behavior, yields for the three intramolecular degrees of freedom (one angle and two O–H bonds) an energy of $(3/2)\ kT$ per molecule (which for 79, 158, and 300 K equals 0.000 375, 0.000 75, and 0.0014 hartree, respectively). The other part of $\langle\Phi^{(1)}\rangle$ corresponds to distortion of the intramolecular HOH angle and O–H bond length. We note also that at a given temperature the value of $\langle\Phi^{(1)}\rangle/n$ increases as the cluster size increases. In addition, we observe that the total dipole moments of the neutral clusters are nonzero and they increase with an increase in the cluster size.

B. Energetics

Following the preparation procedures described above, we have carried out QUPID simulations for a range of cluster sizes at several temperatures and classical molecular dynamics simulations of the corresponding neutral clusters (see Sec. III A and Table I). Results pertaining to the equilibrium energetics of $(H_2O)_n^-$ clusters with the excess electron localized in a surface or interior localization mode are given in Tables II and III, respectively, along with the radius of gyration R_g [Eq. (7)] of the excess electron distribution.

As discussed in the previous section, the formation of a neutral cluster is accompanied by intramolecular structural distortions of the water molecules. The attachment of an electron to a water cluster is accompanied by a reorganization of the intermolecular structure of the cluster compared to the corresponding neutral cluster, while further intramo-

TABLE I. Intra $\langle\Phi^{(1)}\rangle$ and inter $\langle\Phi^{(2)}\rangle$ molecular potential energies, total energies, and total dipole moments for neutral $(H_2O)_n$ cluster, at various temperatures. Energies and dipole moments in units of hartree (1 hartree = 27.212 eV) and $ea_0 = 2.524$ D. Estimated uncertainties (standard deviation of 5 subaverages) are given in square brackets.

n	T(K)	$\langle\Phi^{(1)}\rangle$	$\langle\Phi^{(2)}\rangle$	$\langle\Phi^{(1)}+\Phi^{(2)}\rangle$	$\langle\lvert u\rvert\rangle$
8	79	0.0103	−0.1126	−0.1023[4×10^{-4}]	0.8[0.2]
	158	0.0123	−0.1054	−0.0931[6×10^{-4}]	0.8[0.2]
12	79	0.0168	−0.1859	−0.1691[4×10^{-4}]	1.5[0.2]
	158	0.0193	−0.1728	−0.1535[4×10^{-4}]	1.4[0.2]
18	79	0.0272	−0.3027	−0.2755[3×10^{-4}]	2.6[0.2]
	158	0.0312	−0.2827	−0.2515[5×10^{-4}]	2.6[0.3]
	300	0.0392	−0.2229	−0.1837[5.2×10^{-3}]	1.9[0.7]
32	79	0.0510	−0.5697	−0.5186[1×10^{-3}]	2.9[0.4]
	158	0.0602	−0.5343	−0.4741[3.2×10^{-3}]	2.4[0.6]
	300	0.0742	−0.4569	−0.3826[8.6×10^{-3}]	2.4[1.1]
64	300	0.1500	−0.9411	−0.7911[6.7×10^{-3}]	2.4[1.1]
128	300	0.3015	−2.036	−1.735[7.6×10^{-3}]	4.1[1.5]

TABLE II. Energetics of excess electron localization via surface states in $(H_2O)_n$, at several temperatures. $\langle\Phi^{(1)}\rangle$ and $\langle\Phi^{(2)}\rangle$ are the intra- and intermolecular potential energies, respectively, $\langle\Phi\rangle$ is the total molecular potential energy of the cluster, and E_c is the cluster reorganization energy [Eq. 3(c)]. $\langle V\rangle$ is the potential energy of the excess electron and K_{int} the interaction kinetic energy [see Eq. 2(b)]. EVBE and EABE are the electron vertical and adiabatic binding energies, respectively [Eqs. (4) and (5)], and R_g the radius of gyration of the bead distribution [Eq. (4)]. Energies are in hartree = 2 Ry = 27.212 eV, and length in unit of Bohr radius $a_0 = 0.5218$ Å. Estimated uncertainties (standard deviation of 5 subaverages) are given in square brackets. The number of beads used in the simulations at the various temperatures are 2^{14} (at 20 K), 2^{12} (at 79 K), 2^{11} (at 158 K) and 2^{10} (at 300 K).

n	T(K)	$\langle\Phi^{(1)}\rangle$	$\langle\Phi^{(2)}\rangle$	$\langle\Phi\rangle$	E_c	$\langle V\rangle$	K_{int}	EVBE	EABE	R_g
2	20	0.0006	−0.0100	−0.0094	~0	−0.008	0.0007	−0.0001	−0.0001	≳36
8	79	0.0102	−0.1070	−0.0968 [0.0007]	−0.0055	−0.0212	0.0137	−0.0074 [0.0007]	−0.0020	10.6
	158	0.0126	−0.1006	−0.0880 [0.001]	0.0052	−0.0239	0.0142	−0.0097 [0.001]	−0.0045	9.3
12	79	0.0162	−0.1535	−0.1373 [0.0009]	0.0317	−0.0745	0.0382	−0.0363 [0.0028]	−0.0046	6.0
	158	0.0191	−0.1451	−0.1260 [0.0011]	0.0274	−0.0702	0.0371	−0.0331 [0.0030]	−0.0057	6.0
18	79	0.0258	−0.2523	−0.2265 [0.0004]	0.0490	−0.0920	0.0438	−0.0482 [0.0024]	0.0008	5.5
	300	0.0377	−0.2009	−0.1632 [0.0017]	0.0206	−0.0837	0.0410	−0.0426 [0.0035]	−0.0220	4.7
32	79	0.0512	−0.5314	−0.4802 [0.0070]	0.0385	−0.0815	0.0393	−0.0423 [0.0022]	−0.0038	6.4
	300	0.0712	−0.4120	−0.3408 [0.0069]	0.0418	−0.0827	0.0350	−0.0478 [0.0065]	−0.0059	5.9
64	300	0.1467	−0.8865	−0.7398 [0.0166]	0.0513	−0.1212	0.0512	−0.0700 [0.0050]	−0.0187	5.2

lecular distortions of the water molecules compared to their structure in the corresponding neutral cluster are small. The energetics of the intramolecular structural modifications is reflected in the values of the equilibrium average intramolecular potential energies, $\langle\Phi^{(1)}\rangle$ [with reference to $\langle\Phi^{(1)}\rangle = 0$ in the isolated water molecule] and that of the intermolecular binding is given by $\langle\Phi^{(2)}\rangle$. Comparing the values of $\langle\Phi^{(1)}\rangle$ and $\langle\Phi^{(2)}\rangle$ for the negatively charged clusters (Tables II and III) with the values for the corresponding neutral clusters (Table I), we conclude that the dominant contributions to the cluster reorganization energy E_c (see Tables II and III) originates from intermolecular structural modifications in the cluster due to electron attachment. Furthermore, comparison of E_c for excess electron localization via the formation of surface and interior states (Tables II and III, respectively), shows that for the same cluster size, n, the degree of reorganization, reflected in the magnitude of E_c, is considerably lower for a surface state than for an internal mode of

TABLE III. Energetics of excess electron localization via interior states in $(H_2O)_n$ at several temperatures. The simulations for $n = 8$ denoted by * were performed for a static configuration of the molecules with the structure used in the quantum-chemical all-electron calculations.[30] For meaning of the entries, see caption of Table II.

n	T(K)	$\langle\Phi^{(1)}\rangle$	$\langle\Phi^{(2)}\rangle$	$\langle\Phi\rangle$	E_c	$\langle V\rangle$	K_{int}	EVBE	EABE	R_g
8*	79	0.0045	−0.0174	−0.0129	0.0894	−0.0715	0.0485	−0.0230 [0.0015]	0.0664	6.4
	158	0.0045	−0.0174	−0.0129	0.0802	−0.0744	0.0518	−0.226 [0.0015]	0.0576	6.1
18	79	0.0249	−0.2195	−0.1946 [0.0016]	0.0809	−0.1543	0.0823	−0.0720 [0.0036]	0.0088	4.1
	158	0.0311	−0.2013	−0.1702 [0.0021]	0.0814	−0.1540	0.0857	−0.0683 [0.0038]	0.0131	4.0
32	79	0.0473	−0.4783	−0.4310 [0.0059]	0.0876	−0.1868	0.0984	−0.0884 [0.0035]	−0.0008	4.0
	158	0.0540	−0.4367	−0.3827 [0.0038]	0.0915	−0.1806	0.0941	−0.0865 [0.0051]	0.0050	3.9
	300	0.0700	−0.3632	−0.2932 [0.0101]	0.0894	−0.1777	0.0869	−0.0908 [0.0040]	−0.0014	3.8
64	300	0.1439	−0.8351	−0.6912 [0.0069]	0.0999	−0.2042	0.0866	−0.1176 [0.0041]	−0.0177	3.8
128	300	0.3023	−1.9424	−1.6401 [0.0134]	0.0944	−0.2169	0.0865	−0.1305 [0.0052]	−0.0361	3.9

TABLE IV. Relative contributions to the electron vertical binding energy, EVBE $= K_{int} + \langle V \rangle$ [see Eq. (4)], of the Coulomb, polarization, exclusion and exchange interactions, as well as relative contributions of the total electron potential energy, $\langle V \rangle$, and interaction kinetic energy $\langle K_{int} \rangle$ [see Eq. (3a)]. Equilibrium results are given for various cluster sizes, $(H_2O)_n^-$, at several temperatures. (SS) and (IS) indicate surface state and interior state localization modes, respectively. The value for $n = 8^*$ is for the static $(H_2O)_8^-$ cluster in the configuration used in the all-electron quantum chemical calculations.

n	T(K)	$\frac{\langle V_{Coul} \rangle}{EVBE}$	$\frac{\langle V_p \rangle}{EVBE}$	$\frac{\langle V_e \rangle}{EVBE}$	$\frac{\langle V_x \rangle}{EVBE}$	$\frac{\langle V \rangle}{EVBE}$	$\frac{\langle K_{int}^{Coul} \rangle}{EVBE}$	$\frac{\langle K_{int}^{p} \rangle}{EVBE}$	$\frac{\langle K_{int}^{e} \rangle}{EVBE}$	$\frac{\langle K_{int}^{x} \rangle}{EVBE}$	$\frac{\langle K_{int} \rangle}{EVBE}$
8*	79	3.070	1.183	−2.343	1.200	3.109	−1.630	−0.365	0.378	−0.491	−2.109
8 (SS)	79	2.493	0.760	−0.947	0.533	2.840	−1.120	0.147	−1.067	0.200	−1.840
12 (SS)	79	1.724	0.449	−0.606	0.399	1.966	−0.483	0.152	−0.803	0.168	−0.966
18 (SS)	79	1.702	0.522	−0.767	0.478	1.935	−0.532	0.111	−0.610	0.096	−0.935
(SS)	300	1.720	0.477	−0.664	0.421	1.954	−0.382	0.227	−1.032	0.234	−0.954
(IS)	79	1.831	0.581	−0.848	0.564	2.127	−0.441	0.224	−1.127	0.217	−1.127
32 (SS)	300	1.666	0.459	−0.652	0.386	1.859	−0.498	0.061	−0.473	0.050	−0.859
(IS)	79	1.687	0.676	−0.929	0.606	2.04	−0.439	0.235	−1.056	0.219	−1.040
64 (SS)	300	1.541	0.424	−0.567	0.348	1.747	−0.340	0.138	−0.675	0.129	−0.747
(IS)	300	1.401	0.521	−0.648	0.433	1.708	−0.276	0.178	−0.775	0.165	−0.708
128 (IS)	300	1.374	0.585	−0.628	0.421	1.752	−0.249	0.227	−0.950	0.220	−0.752

localization. Finally, we note that the reorganization energy per molecule (i.e., E_c/n) decreases as the cluster size increases which indicates that the spatial extent of the reorganization region is limited to the neighborhood of the localized electron (more will be said on this question in our discussion of the structural characteristics).

The interaction potential energy of the electron with the host water molecules [$\langle V \rangle$, see Eq. (3b)] is seen to generally increase with the size of the cluster (with the exception of the values for the surface states for $n = 18$ and 32, Table II), and for a given n $\langle V \rangle$ is larger for internal localization than for the surface state. A similar trend is observed for the electron vertical binding energy [EVBE $= K_{int} + \langle V \rangle$, see Eq. (4)]. The values of EVBE for the surface states of $(H_2O)_n^-$ clusters for $n \leqslant 18$ compare well with the values obtained from photoelectron measurements,[39] while the corresponding value for the internal state of $(H_2O)_{18}^-$ is outside the range of the experimental data, and EABE > 0 for this state.

At this point it is of interest to remark on the relative contributions of the four terms in the electron–water interaction potential [V, see Eq. (10)] to the average electron potential energy $\langle V \rangle$ and interaction kinetic energy $\langle K_{int} \rangle$, which together comprise the electron vertical binding energy EVBE. These relative contributions are given in Table IV for the surface and interior states (SS and IS, respectively) for different cluster sizes n at several temperatures. First we note that the relative contribution of $\langle K_{int} \rangle$ to the average electron vertical binding energy (EVBE) is approximately one half that of the electron potential energy $\langle V \rangle$, and of opposite sign (attractive for $\langle V \rangle$ and repulsive for $\langle K_{int} \rangle$). As evident from Table IV, for all cases the dominant contribution to $\langle V \rangle$ is from the Coulomb term (V_{Coul} in the interaction potential) with the next largest contribution coming from the repulsion due to the exclusion potential (V_e). The attractive contributions to $\langle V \rangle$ from the polarization $\langle V_p \rangle$ and exchange $\langle V_x \rangle$ are of comparable magnitudes. The largest contribution to $\langle K_{int} \rangle$ is due to the exclusion term $\langle K_{int}^e \rangle$, followed by the contribution due to Coulomb interaction $\langle K_{int}^{Coul} \rangle$, with smaller and comparable in magnitude contribution from the polarization and exchange terms, $\langle K_{int}^p \rangle$ and $\langle K_{int}^x \rangle$, respectively. The large relative contribution of the exclusion term to $\langle K_{int} \rangle$, reflects the fact that the evaluation of K_{int} involves the gradient of the potential [see second term on the right-hand side of Eq. (3a)] and as can be seen from our discussion of the electron–water interaction potential (see paper I, Sec. II), the repulsive exclusion term exhibits the fastest spatial variation.

The energetic stability of the equilibrium negatively charged cluster with respect to the equilibrium neutral clusters plus free electron is inferred from the magnitude and sign of the electron adiabatic binding energy [EABE, see Eq. (5)], with a negative value corresponding to a stable bound state. The values of EABE are a consequence of a balance between the electron vertical binding energy, EVBE, and the cluster reorganization energy E_c. As seen from Table II the surface states for cluster sizes $n \leqslant 18$ are characterized by negative EABE values (the small value for $n = 18$ at $T = 79$ K is within the calculational error). The corresponding EABE's for electron internal states are all positive precluding a stable internal localization mode for $n \leqslant 18$. In fact, we were unable to form an interior localized excess electron state in clusters with $n = 8$ or 12. The absence of 300 K data for $n = 8$ and 12 surface states is due to the fact that no excess electron–water cluster bound state was found by us upon heating the lower temperature $(H_2O)_n^-$ clusters to that temperature. Similarly no data are given for an interior state (IS) for $n = 18$ at 300 K since upon heating the equilibrated IS $(H_2O)_{18}^-$ cluster from 158 to 300 K the mode of localization converted to a surface state. We should also remark that the inability to structurally anneal the surface state clusters for $n < 18$ at high temperature (which would have enhanced the molecular motions and allow for optimization of the molecular reorganization processes) may cause these negative charged clusters to be not fully relaxed which would result in E_c, as well as EABE, values which are upper bounds to the optimum values. For this reason our equilibration calculations, particularly for these low temperature clusters, were rather time consuming.

To estimate the initial binding of an electron to an equilibrated neutral cluster, and to confirm the thermodynamic

TABLE V. Dipole moments $\langle|\mu|\rangle$ of equilibrium molecular clusters $(H_2O)_n^-$, not including the excess electron, and average values of the H–O–H angle, $\langle\theta\rangle$, and O–H bond length $\langle R_{OH}\rangle$, for various cluster sizes at several temperatures. The corresponding values for an isolated water molecule are $\mu = 0.74\, ea_0$, $\theta = 104.52°$, and $R_{OH} = 1.809\, a_0$. The dipole moments are in units of ea_0 (= 2.524 D). For comparison with the dipole moments of the corresponding neutral $(H_2O)_n$ clusters, see Table I. (SS) and (IS) indicate surface state and interior state localization modes, respectively. The value for $n = 8^*$ is for the static $(H_2O)_8$ cluster in the configuration used in the all-electron quantum chemical calculations. Standard deviations are given in parentheses.

n	T(K)	$\langle\|\mu\|\rangle$	$\langle\theta\rangle$	$\langle R_{OH}\rangle$
8*	158	1.6	109.0	1.795
8 (SS)	79	3.6 (0.2)	104.4 (2.5	1.846 (0.031)
12 (SS)	79	5.4 (0.1)	104.2 (2.5)	1.849 (0.031)
18 (SS)	79	5.1 (0.2)	104.1 (2.5)	1.850 (0.031)
(SS)	300	4.3 (0.7)	103.9 (4.7)	1.841 (0.048)
(IS)	79	2.2 (0.2)	104.4 (2.7)	1.848 (0.030)
32 (SS)	300	8.9 (1.0)	104.4 (4.7)	1.844 (0.049)
(IS)	79	1.9 (0.4)	104.1 (2.6)	1.851 (0.029)
(IS)	300	2.0 (0.8)	104.2 (4.8)	1.843 (0.049)
64 (SS)	300	12.4 (1.5)	104.7 (4.8)	1.844 (0.049)
(IS)	300	2.9 (1.2)	104.4 (4.6)	1.843 (0.048)
128 (IS)	300	6.3 (1.7)	104.7 (4.7)	1.847 (0.049)

stability of the excess electron surface states for $n < 18$, we first attempted to equilibrate a system consisting of 12 *static* water molecules (in an equilibrium neutral cluster configuration) plus an excess electron. The EVBE for this system was positive for $T \geqslant 79$ K, but at $T = 20$ K we obtained a very diffuse bound electron state with EVBE $\approx -2\times10^{-4}$ hartree ($\approx$5 meV). Subsequently, we allowed the water molecules to evolve dynamically, heated the system to 150 K, and observed that the isomorphic system slowly developed from the diffuse, low EVBE state toward a localized bound surface state similar to that obtained by the preparation method described above. Thus, we conclude that a neutral equilibrated $(H_2O)_{12}$ cluster can weakly bind an electron with little or no molecular reorganization and that the free-energy barrier from this initial diffuse and marginally bound state to the localized surface state, characterized by EVBE ≈ -0.035 hartree, can be overcome when cluster molecular reorganization becomes operative. These observations relate to the alternative experimental methods of preparation of negatively charged clusters,[35–41] particularly to the capture of very low energy electrons by cold water clusters.[40,41]

With increase in the size of the water cluster the internal localization mode becomes more energetically favored as can be seen by comparing the EABE values given in Table II and III for the surface and internal states, respectively, of $(H_2O)_n^-$ for $n > 18$. It is observed that as the cluster size increases the electron vertical binding energies (EVBE) become larger in magnitude (and are larger for the internal states than for the surface states) and the EABE's are all negative for clusters in this size range (the EABE's for the IS and SS for $n = 32$ and 64 are comparable to within the uncertainty of the calculation). We also note that even for the large $(H_2O)_{128}^-$ cluster the value of EABE (-0.036 hartree $= -0.98$ eV) is significantly below the estimated experimental heat of solution (hydration) of an electron in bulk water, $\Delta H(e_{eq}^-) = -1.7$ eV. This indicates that while the internal electron localization in large water clusters may be regarded as a precursor of the hydrated electron in bulk water, the convergence to the bulk limit is rather slow, which is a manifestation of the role of long-range interactions in electron solvation in polar solvents.

These results suggest that the transition from surface to interior excess electron localization in water clusters occurs in the range of $32 < n \lesssim 64$. A decisive determination of the localization mode for this cluster size range may rest on the experimental determination of EVBE from photoelectron spectra, since the predicted values are markedly different for the two localization modes (compare Tables II and III, for $n > 32$).

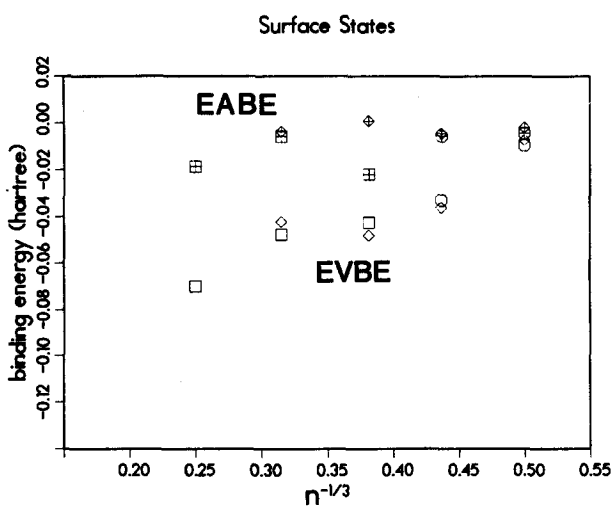

FIG. 1. Plots of the electron vertical binding energies (EVBE) and electron adiabatic binding energies (EABE), for surface states of an excess electron in $(H_2O)_n^-$ clusters, vs $n^{-1/3}$. For EVBE the square, hexagon, and diamond symbols correspond to results at 300, 158, and 79 K, respectively. The same symbols but with a cross inside are used for EABE.

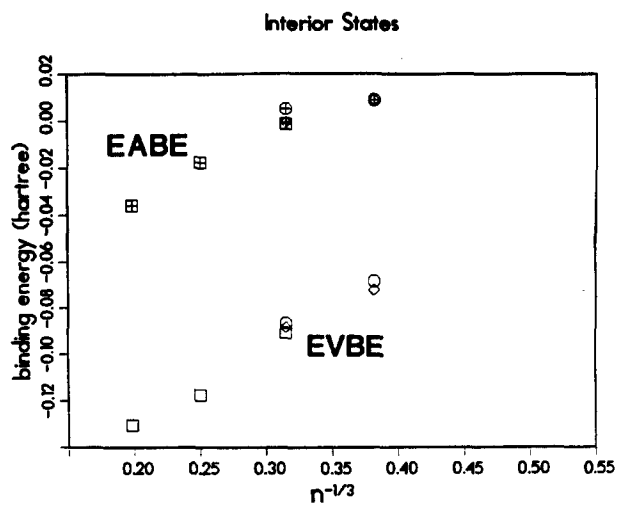

FIG. 2. Plots of electron vertical binding energies (EVBE) and electron adiabatic binding energies (EABE), for interior states of an excess electron in $(H_2O)_n^-$ clusters, vs $n^{-1/3}$. Note the linear relationship. Symbols as in caption to Fig. 1.

The results for the EVBE's and EABE's for the surface and internal states are summarized in Figs. 1 and 2, respectively, where the values at several temperatures are plotted vs $n^{-1/3}$. The motivation for the $n^{-1/3}$ dependence originates from consideration of the expression for the binding energy of an excess electron in a dielectric sphere. The energetics of a charge distribution in the presence of a dielectric medium[69] and dielectric medium effects on a loosely bound electron[70] have been studied at the early stages of development of the theory of solvation. In the following we adapt the expressions for the binding energies obtained in these early studies to our finite cluster system. From the definitions of the electron adiabatic and vertical binding energies [Eqs. (5) and (4), respectively], and the total energy expression given by Eq. (35) of Ref. 70, and assuming spherical symmetry and uniform dielectric properties, the following expression for EABE is obtained:

$$\text{EABE} = K_{\text{int}} - \frac{1}{2}\left[1 - D_s^{-1}\right] \int_0^{\bar{R}} r^2\, dr\, E_e(r)^2, \tag{11a}$$

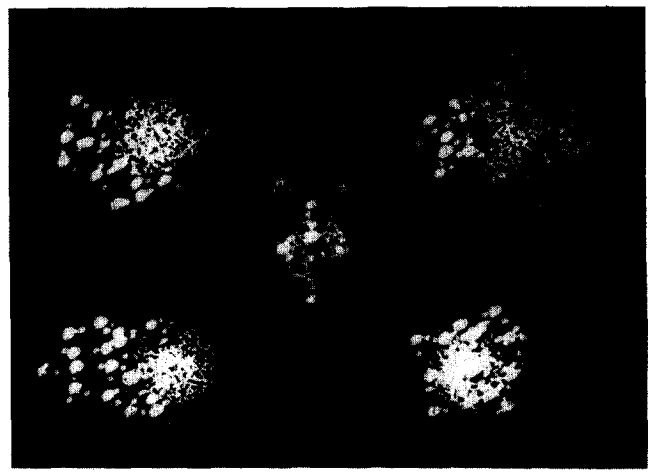

FIG. 3. Cluster configurations of $(H_2O)_n^-$, via quantum path-integral molecular dynamics simulations. The large and small balls correspond to oxygen and hydrogen, respectively. The dots represent the electron (bead) distributions. Shown at the center is $(H_2O)_8^-$, for a static molecular configuration as in Ref. 30. From top right and going counterclockwise: (i) diffuse surface state of $(H_2O)_8^-$; (ii) surface state of $(H_2O)_{12}^-$; (iii) surface state of $(H_2O)_{18}^-$ and (iv) internal state of $(H_2O)_{18}^-$.

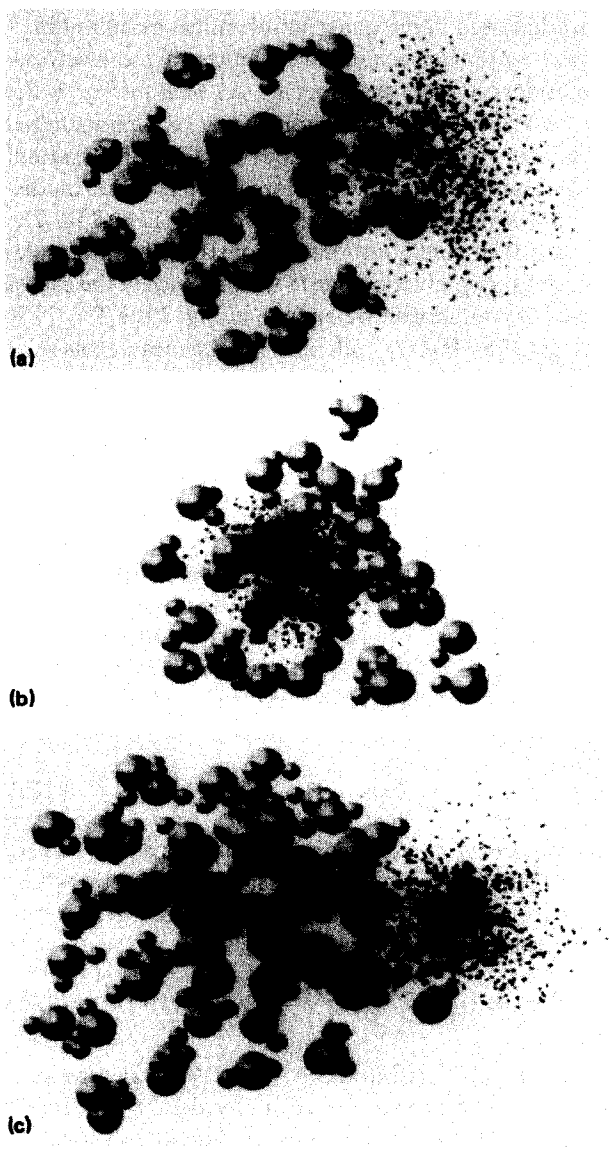

FIG. 4. Cluster configurations of $(H_2O)_n^-$ obtained via quantum path-integral molecular dynamics simulations. Large and small balls correspond to oxygen and hydrogen atoms, respectively. The dots represent the electron (bead) distributions. (a) Surface state in $(H_2O)_{32}^-$; (b) internal state in $(H_2O)_{32}^-$; (c) surface state in $(H_2O)_{64}^-$; (d) internal state in $(H_2O)_{64}^-$; (e) internal state in $(H_2O)_{128}^-$. All calculations were performed at 300 K.

where D_s is the static dielectric constant, $K_{\rm int}$ is as defined in Eq. (3a), $\overline{R}$ is the radius of the dielectric sphere, and $E_e(r)$ is the magnitude of the electric field due to the excess electron distribution $\rho(r)$. To obtain the expression for EVBE the reorganization energy, E_c [see Eq. (6)], has to be subtracted from EABE [see Eq. (5)]. In the dielectric continuum theory, the quantity corresponding to E_c is the energy change involved in a transformation of a neutral dielectric sphere, in which both the electronic and molecular orientation components of the polarization field are in equilibrium, to a nonequilibrium state of the neutral dielectric sphere in which only the electronic component is in equilibrium while the orientational component of the polarization field has the value it had in the equilibrium negatively charged system. Thus, using Eq. (15) of Ref. 70 in conjunction with Eq. (11a) we obtain

$$\text{EVBE} = \text{EABE} - \frac{1}{2}\left[D_{\rm op}^{-1} - D_s^{-1}\right] \times \int_0^{\overline{R}} r^2\, dr\, E_e(r)^2, \tag{11b}$$

where $D_{\rm op}$ is the optical dielectric constant.

To establish the linear dependence of EVBE (and EABE) on $n^{-1/3}$, we evaluate the integral in Eq. (11b) for a compact, localized, excess electron charge distribution, which is the case for our internally localized states (see pictures of the cluster configurations and electron distributions in Figs. 3 and 4 and values of the radii of gyration of the excess electron distributions R_g in Table III). Under these conditions $\rho(r) = 0$ for $r > R_1$, where $R_1 < \overline{R}$, and for $r > R_1$ the electric field is given by

$$E_e(r) = \frac{1}{r^2}\int d^3 r'\, \rho(r') = e/r^2. \tag{11c}$$

Using Eq. (11c) in the integral in Eqs. (11a) and (11b) yields

$$\int_0^{\overline{R}} r^2\, dr\, E_e(r)^2 = \int_0^{R_1} r^2\, dr\, E_e(r)^2 + \int_{R_1}^{\overline{R}} r^2\, dr (e/r^2)^2 \equiv \epsilon_{R_1} - \frac{e^2}{\overline{R}}. \tag{11d}$$

Making the further assumption that $K_{\rm int}$ and $\rho(r)$ do not depend on the cluster size, which is consistent with the results of the simulations for $K_{\rm int}$ and R_g given in Table III, we get

$$\text{EVBE} = K_{\rm int} - \tfrac{1}{2}\left(1 + D_{\rm op}^{-1} - 2D_s^{-1}\right)\left(\epsilon_{R_1} - \overline{R}^{-1}\right) = A + Bn^{-1/3}, \tag{11e}$$

where $B = (1 + D_{\rm op}^{-1} - 2D_s^{-1})e^2/(2R_s)$, and R_s is the effective radius of a solvent molecule. An estimate of R_s can be obtained from the average density of molecules in the interior of the larger water clusters studied by us yielding a value of $R_s \approx 3.5\ a_0$. With this value of R_s, and taking[14] $D_{\rm op} = 1.78$, $D_s = 78.5$ (at 298 K) we obtain $B = 0.21$ hartree for the slope of EVBE vs $n^{-1/3}$ (using[14] $R_s = 2.8\ a_0$ yields $B = 0.26$ hartree). Inspection of Fig. 2 reveals that both EABE and EVBE obtained via our simulations exhibit a linear dependence on $n^{-1/3}$ as predicted by the above considerations. However, one should bear in mind the simplifying assumptions underlying the dielectric response model in comparing the predictions for A and B with the simulation results. For the surface states, Fig. 1, no such clear linear dependence on $n^{-1/3}$ is seen, reflecting the lack of spherical symmetry of the host medium about the localized excess electron and a larger dependence on the local environment for the different clusters. Finally we remark that the reorganization energy E_c can be read from Figs. 1 and 2 as the energy difference between EABE and EVBE [see Eq. (5)].

C. Structure

The energetics and structure of our systems are intimately related to each other. In this section we discuss the structural aspects of the excess electron states in $(H_2O)_n^-$, in light of our discussion of the underlying energetics given in Sec. III B. A pictoral representation of the configurations of excess electron states of $(H_2O)_n^-$ clusters ($n \leqslant 18$) is given in Fig. 3, and for $n \geqslant 32$ in Fig. 4 (in addition we show in the middle of Fig. 3 the $(H_2O)_8^-$ cluster in the static molecular configuration used in the quantum-chemical calculations,[30] which was employed in the construction of the electron–water pseudopotential, see paper I). As seen in Fig. 3, the $(H_2O)_8^-$ surface state (upper right corner) is characterized by a diffuse electron distribution (radius of gyration, $R_g = 10\ a_0$, see Table II), with more compact electron distributions (see R_g values in Table II) for $n = 12$ and 18. The cluster molecular configurations demonstrate the intermolecular cluster reorganization due to the presence of the excess electron. For comparison we include in Fig. 3 the $T = 79$ K internal state for $(H_2O)_{18}^-$, which is not the most stable state for this cluster (positive EABE, see Table III). The internal states for $n = 32$, 64, and 128 shown in Fig. 4 demonstrate the high degree of electron localization in these states. It is also of interest to note the development of hydrogen-bonded rings which are characteristic to frozen water structures.

Detailed structural information for the various clusters is provided by the histograms of the number radial distributions shown in Fig. 5–7. Shown in these figures are the radial number distributions of the oxygen and hydrogen atoms (positions $\mathbf{R}_{I,\alpha}$; α = O,H respectively) with respect to the *barycenter* of the isomorphic electron bead distribution ($\mathbf{r}_{\rm ebc}$)

$$n_{{\rm ebc}-\alpha}(r) = \left\langle \sum_{I=1}^{n} \delta(r - |\mathbf{R}_{I,\alpha} - \mathbf{r}_{\rm ebc}|) \right\rangle. \tag{12a}$$

Also shown are the corresponding distributions with respect to the electron distribution (i.e., the individual beads, whose locations are denoted by $\mathbf{r}_j$ ($j = 1,\ldots,P$) where P is the number of beads used in the calculation),

$$n_{e-\alpha}(r) = \left\langle \frac{1}{P}\sum_{j=1}^{P}\sum_{I=1}^{n} \delta(r - |\mathbf{R}_{I,\alpha} - \mathbf{r}_j|) \right\rangle. \tag{12b}$$

For the hydrogen distribution functions (α = H) the sum includes both hydrogens of each molecule. In converting Eqs. (12a) and 12b) to histograms, as shown in the figures,

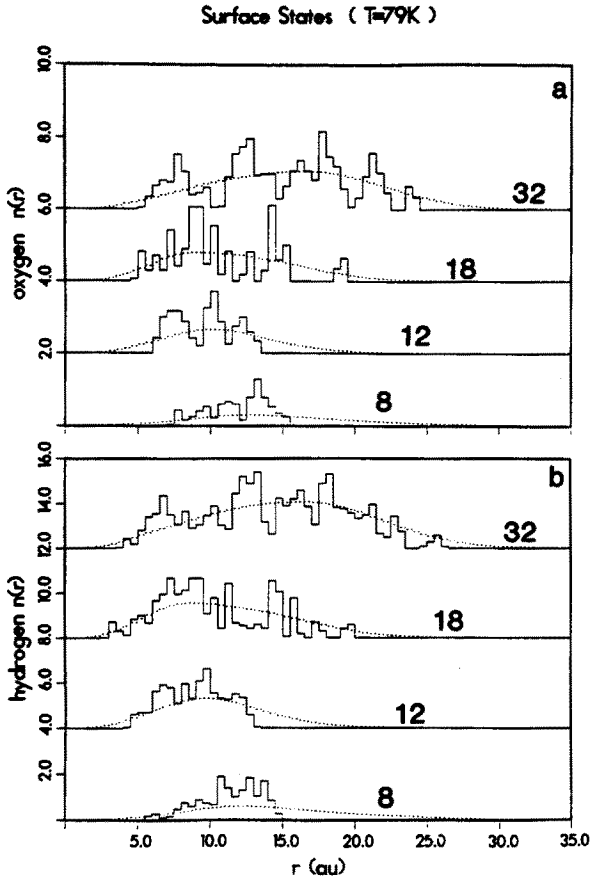

FIG. 5. Histograms of the number radial distributions $n(r)$ for oxygens (a) and hydrogens (b), for the surface states of $(H_2O)_n^-$ clusters ($n = 8$, 12, 18, and 32) at $T = 79$ K. The solid lines correspond to the radial distributions between the barycenter of the (isomorphic) electron distribution and the atoms, and the dashed lines correspond to the radial distribution between the isomorphic) electron distribution (beads) and the atoms.

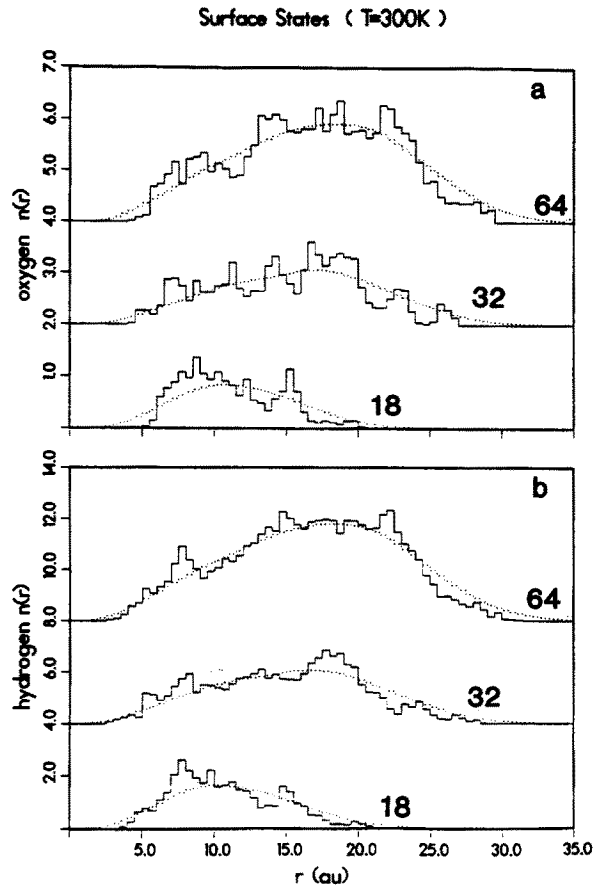

FIG. 6. Same as Fig. 5, for surface states of $(H_2O)_n^-$ clusters, $n = 18$, 32, and 64, at $T = 300$ K.

we use a bin width of 0.5 a_0. The angular brackets indicate average over electron (isomorphic necklace) and nuclear configurations obtained via the simulation. In general $n_{e-\alpha}(r)$ (dashed line) appears as a smoothed version of the $n_{\text{ebc}-\alpha}(r)$ function, and provides a characterization of the excess electron distribution relative to the atomic constituents of the host cluster. Inspection of $n_{\text{ebc}-\alpha}(r)$ for the surface states of $(H_2O)_n^-$ for $n = 8 - 32$ at 79 K (Fig. 5), demonstrates the diffuseness of the electron distribution in these states. Comparison of the number radial distributions for the oxygens and hydrogens [Figs. 5(a) and 5(b), respectively] shows that the hydrogens of the water molecules nearest to the excess electron are closer to the barycenter of the electron distribution than the oxygens by 1–2 a_0. This observation applies to all the negatively charged clusters (see Figs. 5–7). For the surface states of the smaller clusters, ($n \leqslant 32$) we observe (see Fig. 5) that the distance of the closest approach of the water molecules to the barycenter of the electron distribution decreases with increasing cluster size. We also note that for the surface states (Figs. 5 and 6) there is no clear indication of a shell structure of the water molecules about the excess electron. For the higher temperature clusters the number radial distribution functions are less structured, due to the thermal motion of the molecules) (compare Figs. 5 and 6).

Inspection of Fig. 7, for the internal localization mode, reveals that the radius of the internal cavity containing the electron is independent of cluster size (consistent with the radii of gyration R_g given in Table III). In contrast to the absence of clear structural features of the host cluster for the surface states, the $n_{\text{ebc}-\alpha}$ radial distribution functions exhibit minima, for all cluster sizes, at $\sim 10\, a_0$, establishing a molecular shell structure about the localized electron. There are typically about 20 molecules within the $10\, a_0$ radius. The radius of the sphere around the barycenter of the electron distribution which contains six oxygens is 7.0–7.5 a_0. Indeed, inspection of $n_{\text{ebc}-0}$ [Fig. 7(a)] suggests the existence of a molecular shell of this radius.

Further evidence for the shell structure of the host cluster is provided by the spatial distribution of the electron–water interaction potential energy, an example of which is shown in Fig. 8 for the surface and internal states of $(H_2O)_{64}^-$, at 300 K. The function displayed in this figure is given by

$$\text{PE}_{e\text{-}H_2O}(r) = \left\langle \sum_{I=1}^{n} \frac{1}{P} \sum_{j=1}^{P} V(\mathbf{r}_j, \{\mathbf{R}_{I,\alpha}\}) \delta(r - |\mathbf{R}_{I0} - \mathbf{r}_{\text{ebc}}|) \right\rangle, \tag{13}$$

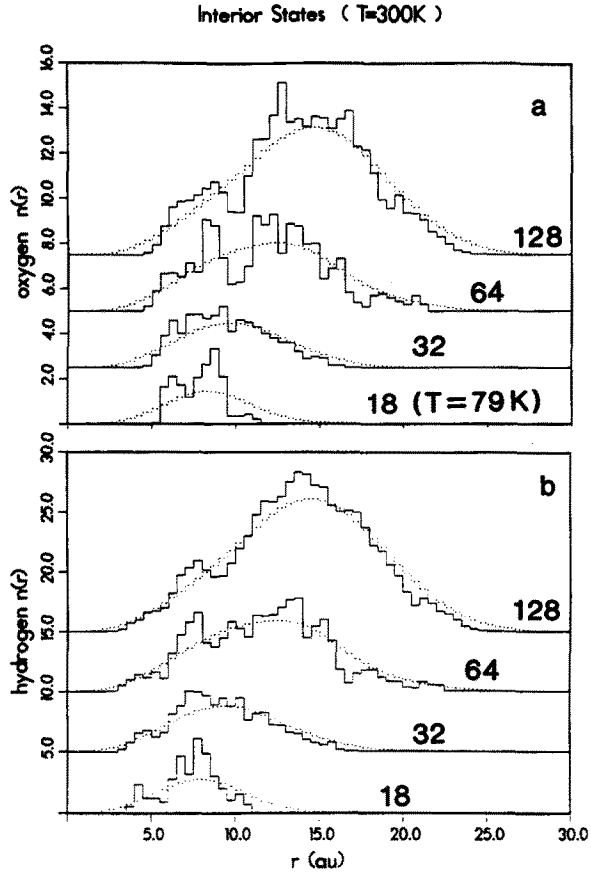

FIG. 7. Same as Fig. 5, for internal states of $(H_2O)_n^-$ clusters, $n = 18$, 32, 64, and 128. The data for $n = 18$ is for $T = 79$ K, all the other data at $T = 300$ K.

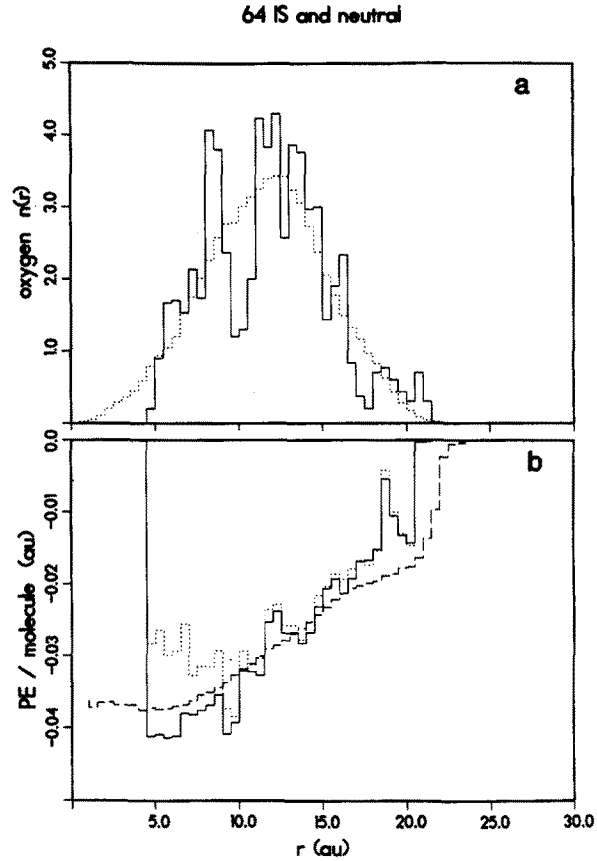

FIG. 9. (a) The radial distribution function, n_{ebc-O}, for $(H_2O)_{\bar{64}}$ at 300 K (solid line) and the radial distribution function of the oxygen atoms with respect to the molecular barycenter of the neutral cluster at 300 K (dotted line). (b) The solid line represents the radial distribution of the molecular vertical binding energy (MVBE) of a water molecule, i.e., the negative of the average energy required to remove an H_2O molecule (whose oxygen is a distance r from r_{ebc}) from the cluster without allowing molecular or electron relaxation, for $(H_2O)_{\bar{64}}$ at 300 K. The contribution to MVBE from the intermolecular interactions, i.e., excluding the electron–water interaction is represented by the dotted line. The dashed line represent MVBE of the neutral, $(H_2O)_{64}$, cluster at 300 K, with the origin at the molecular barycenter. The per molecule cluster reorganization energy is reflected in the energy difference between the dotted and dashed lines.

where $R_{I,\alpha}$ ($\alpha = 0$, H1, H2) are the positions of the oxygen and hydrogen atoms of the I th water molecule, respectively, and $\mathbf{r}_j$ ($j = 1,...P$) is the position of the jth pseudoparticle (bead). As evident from the figure, the internal state (IS) exhibits minimum interaction energies at 7.5 a_0 and 10 a_0,

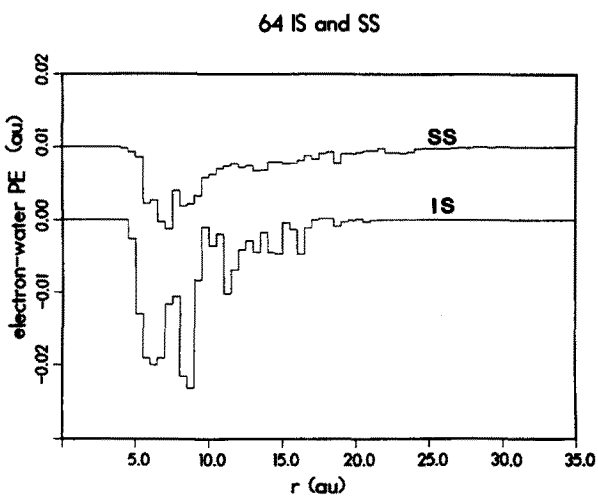

FIG. 8. Radial distribution of the electron–water interaction potential energy, see Eq. (13), for the surface (SS) internal (IS) states of the $(H_2O)_{\bar{64}}$ cluster at 300 K. Note the minima in the magnitude of the interaction energy for IS at $r = 7.5\ a_0$ and $10\ a_0$. Energy in a.u. (hartree).

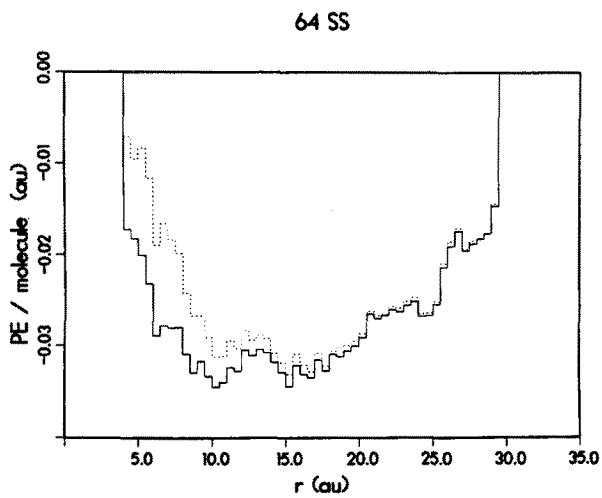

FIG. 10. The radial distribution of the molecular vertical binding energy [MVBE, see Eq. (15)] of a water molecule (solid line) and the contribution to MVBE from the intermolecular interactions (dotted line) for the surface state of $(H_2O)_{\bar{64}}$ at 300 K.

which correlate with the molecular shell structure discussed above.

In Fig. 9(a) we compare the radial distribution function, $n_{\mathrm{ebc}-0}$ for $(H_2O)_{64}^-$, represented by the solid line, with the radial distribution of the oxygen atoms in the neutral cluster with respect to the molecular barycenter. First we observe that the spatial dimensions of the two clusters are comparable. Second, the reorganization of the cluster, due to the attachment of the electron in an internal localization mode, into a molecular shell structure, is apparent. To facilitate analysis of the spatial extent of the excess electron–water interaction and of the resulting molecular reorganization of the host cluster, we define, in addition to the function $\mathrm{PE}_{e\text{-}H_2O}(r)$ given in Eq. (13), the following functions: (i) The intermolecular interaction radial distribution function,

$$\mathrm{PE}_{H_2O\text{-}H_2O}(r) = \left\langle \sum_{I=1}^{N} \frac{1}{2} \sum_{\substack{J=1 \\ J\neq I}}^{N} \phi^{(2)}(\{\mathbf{R}_{I,\alpha}\},\{\mathbf{R}_{J,\alpha}\}) \times \delta(r - |\mathbf{R}_{I,0} - \mathbf{r}_{\mathrm{ebc}}|) \right\rangle, \tag{14}$$

where $\Phi^{(2)}$ is the intermolecular interaction potential between water molecules [see Eq. (1) and Sec. III of paper I], and (ii) the molecular vertical binding energy (MVBE) radial distribution function,

$$\mathrm{MVBE}(r) = [2\mathrm{PE}_{H_2O\text{-}H_2O}(r) + \mathrm{PE}_{e\text{-}H_2O}(r)]/n_{\mathrm{ebc}-0}(r). \tag{15}$$

MVBE(r) is the negative of the average energy required to remove from the cluster an H_2O molecule, whose oxygen is located at a distance r from the excess electron barycenter, without allowing molecular and electronic relaxation. These functions [with $\mathrm{PE}_{H_2O\text{-}H_2O}(r)$ divided by $\frac{1}{2}n_{\mathrm{ebc}-0}(r)$] are shown in Fig. 9(b) as well as the radial distribution of the intermolecular interactions in the neutral cluster, which is obtained from Eq. (14) by replacing $\mathbf{r}_{\mathrm{ebc}}$ by the molecular barycenter $\mathbf{r}_{\mathrm{mbc}}$, and is normalized by dividing by the corresponding oxygen radial distribution function. The per molecule cluster reorganization energy is reflected in the energy difference between the dashed and dotted curves in Fig. 9(b). As seen from Figs. 8 and 9, the spatial extent of the interaction between the excess electron and the water molecules and the resulting molecular reorganization is largely contained within a sphere of radius 10 a_0 (note that beyond this distance all three curves follow each other, except for $r > 18\ a_0$ where only a few water molecules are found). For comparison, the MVBE and $\mathrm{PE}_{H_2O\text{-}H_2O}$ distributions for the surface state of the $(H_2O)_{64}^-$ cluster are shown in Fig. 10 (the corresponding neutral cluster MVBE curve is not shown). Figures 8 and 10 illustrate that the excess electron–water molecule interaction is also largely contained within a radius of 10 a_0 about the electron barycenter for the surface state although the division is much less pronounced.

Additional information and insight pertaining to the local structure of the host cluster in the presence of the excess electron is obtained from the bond and dipole orientational correlation functions $P(\cos\theta_{\mathrm{bond}})$ and $P(\cos\theta_{\mathrm{dipole}})$. The correlation functions are defined by

$$P_{\mathrm{shell}}(X) = \frac{1}{\langle N\rangle}\left\langle \sum_{I\in \mathrm{shell}} \delta(\cos\theta_I - X)\right\rangle, \tag{16}$$

where the sum is over all molecules within the specified shell [and over both O–H bonds in the case of $P(\cos\theta_{\mathrm{bond}})$], and $\langle N\rangle$ is the average number of terms in the sum. The bond angle is defined by

$$\cos(\theta_{\mathrm{bond}}) = (\mathbf{R}_{I,\mathrm{H}} - \mathbf{R}_{I,0})\cdot(\mathbf{r}_{\mathrm{ebc}} - \mathbf{R}_{I,0})/ |\mathbf{R}_{I,\mathrm{H}} - \mathbf{R}_{I,0}||\mathbf{r}_{\mathrm{ebc}} - \mathbf{R}_{I,0}|. \tag{17}$$

The dipole angle θ_{dipole} is obtained by replacing $(\mathbf{R}_{I,\mathrm{H}} - \mathbf{R}_{I,0})$ in Eq. (17) with a vector in the direction of the molecular dipole (see paper I). The shells are defined to contain all the molecules whose oxygens are located in the interval (r_-, r_+) between the two shell radii. In choosing the

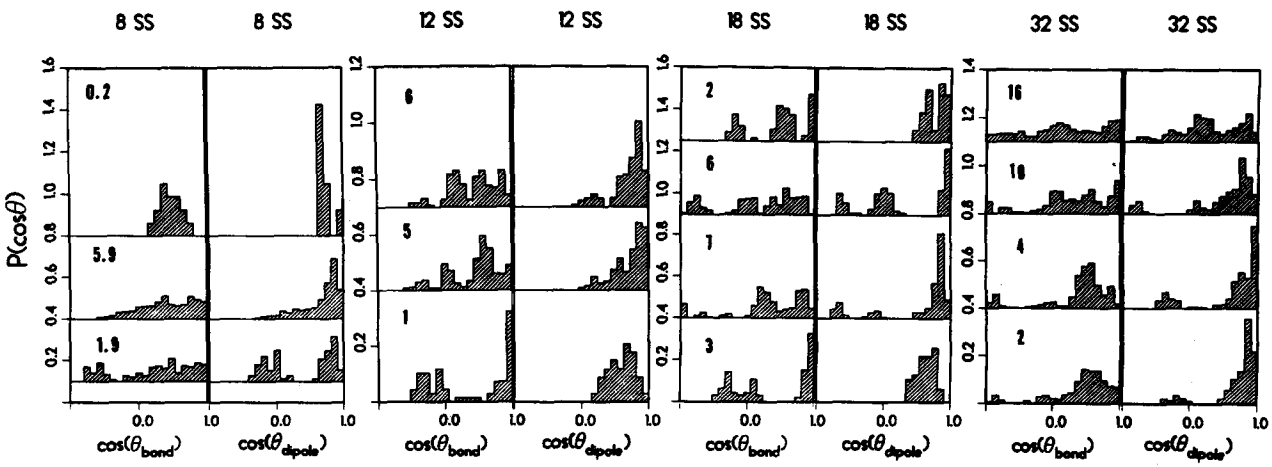

FIG. 11. Orientational correlation functions, $P(\cos\theta)$ vs $\cos\theta$, for the surface states of $(H_2O)_n^-$ clusters ($n = 8$, 12, 18, and 32) at $T = 79$ K. For each cluster size we show on the left the correlation function of OH bond directions with respect to the vector connecting the oxygen atom with the barycenter of the excess electron distribution, and on the right the correlation function between that vector and the molecular dipole. Histograms are shown for the correlation functions averaged over molecules in shells. The shell radii from the bottom of the figure and up are (0,7 a_0), (7 a_0, 10 a_0), (10 a_0, 15 a_0), and (15 a_0, ∞). The average number of molecules (rounded in most cases to the nearest integer) within each shell are given in the figure.

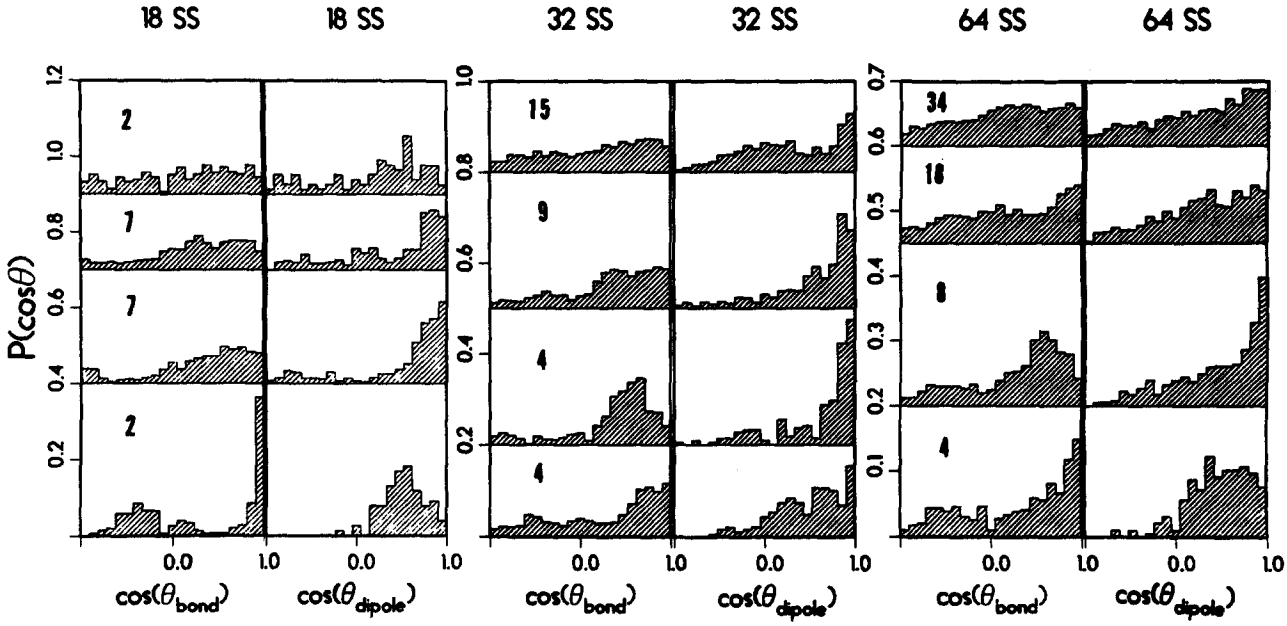

FIG. 12. Orientational correlation functions, $P(\cos\theta)$ vs $\cos\theta$, for the surface states of $(H_2O)_n^-$ clusters (n = 18, 32, and 64) at $T = 300$ K. For details see caption to Fig. 11.

shell radii we were guided by the molecular shell structure discussed above: (0,7 a_0), (7 a_0, 10 a_0), (10 a_0, 15 a_0), and (15 a_0, ∞). While the values for the first two shells are based on our structural analysis, the value of 15 a_0 was selected since it is approximately the radius of the $n = 32$ cluster.

We note that when one of the OH bonds of a molecule points toward the barycenter of the electron distribution [i.e., $\cos(\theta_{\text{bond}}) = 1$] the other OH bond is oriented such that $\cos(\theta_{\text{bond}}) = -0.25$, and $\cos(\theta_{\text{dipole}}) = 0.61$; while when $\cos(\theta_{\text{dipole}}) = 1$, i.e., dipole orientation then $\cos(\theta_{\text{bond}}) = 0.61$.

For the low-temperature surface states (Fig. 11) of the small cluster sizes ($n<32$) we observe that the degree of bond versus dipole orientation (with respect to the barycenter of the excess electron distribution) depends on the cluster size, and for a given cluster on the distance (i.e., shell number) from the localized electron. For the smallest cluster, $n = 8$, no molecules are found in the first (0–7 a_0) shell. The orientation in the other shells is mainly dipole oriented. For the surface states of the larger clusters ($n > 8$), dipole orientation predominates, although with increasing cluster size we observe an increased tendency for bond orientation of the molecules in the innermost shells (see Figs. 11 and 12). The latter observation correlates with the more compact nature of the excess electron distribution in the larger cluster surface states. Comparison of the orientational correlation functions for the low and high temperatures given in Figs. 11 and 12, respectively, demonstrates that the increased molecular motions at the higher temperature results in a more uniform distribution over angles.

Inspection of Fig. 13 reveals that for the internal states of all cluster sizes ($n \geqslant 18$) the innermost shell contains six

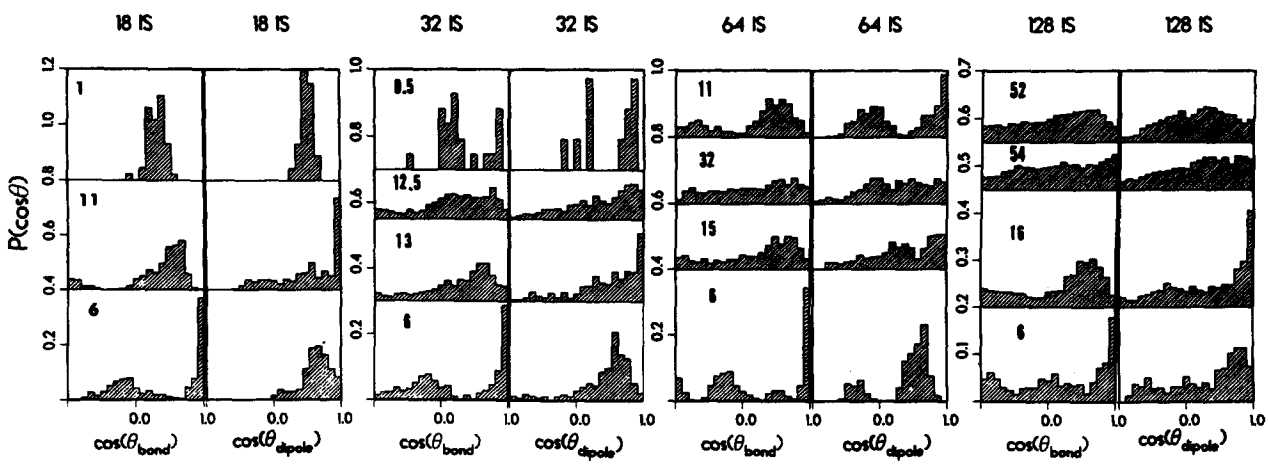

FIG. 13. Orientational correlation functions, $P(\cos\theta)$ vs $\cos\theta$, for the interior states of $(H_2O)_n^-$ clusters ($n = 18$, 32, 64, and 128). With the exception of the $n = 18$ cluster whose temperature is 79 K, all other clusters are at 300 K. For details see caption to Fig. 11.

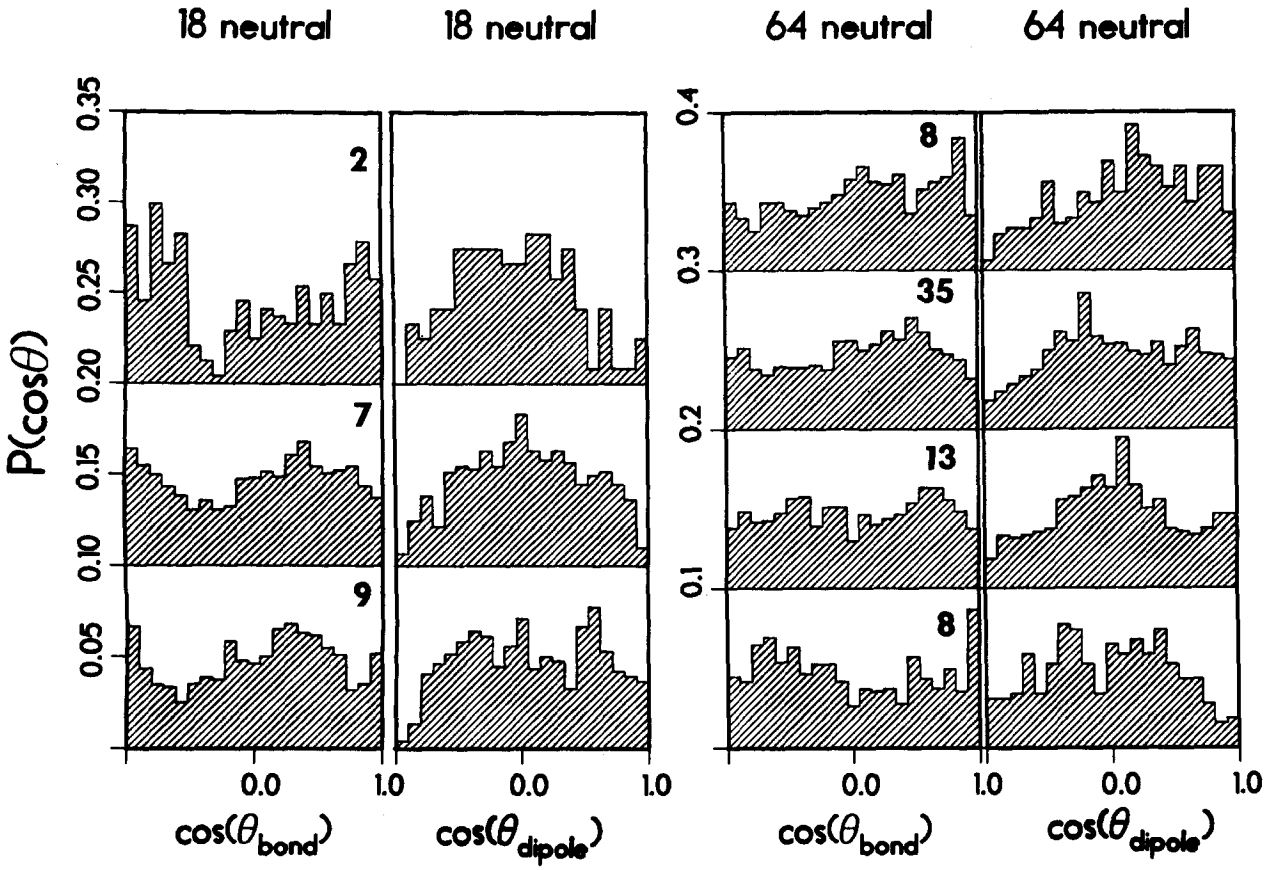

FIG. 14. Orientational correlation functions, $P(\cos\theta)$ vs $\cos\theta$, for neutral $(H_2O)_n^-$ clusters ($n = 18$ and 64), at $T = 300$ K. The bond and dipole correlations are with respect to the molecular barycenter of the cluster.

molecules which are bond oriented, in agreement with results obtained via simulations of electron hydration in bulk water[26,27] and the experimental results obtained via studies of alkaline ice glasses.[33,34] In the second shell a predominance of dipole-orientation is seen. In the outer shells the distribution is more uniform with a bias toward positive values of both $\cos(\theta_{\text{bond}})$ and $\cos(\theta_{\text{dipole}})$. The molecular orientations in the outer shells is influenced not only by the long-range interaction with the excess electron, but also by the cooperative interaction with the molecules in the inner shells.

Finally, for comparison and in order to highlight the influence of the excess electron on the structure of the host cluster, we display in Fig. 14 the orientational correlation functions for the neutral $(H_2O)_{18}$ and $(H_2O)_{64}$ clusters (at 300 K). Here, the bond and dipole correlations are calculated with respect to the molecular barycenter of the cluster. As evident from Fig. 14, the distributions are rather uniform with no particular bias toward positive or negative value of $\cos\theta$.

D. Electronic properties and excitations

In the previous subsections we discussed the energetics and structure of excess electron localization in water clusters. We focus now on aspects related to properties of the localized electron.

As mentioned in Sec. II the degree of localization of the excess electron can be characterized by the complex time correlation (or response) function[15,27] [see Eq. (8)] which can be expressed as

$$\mathcal{R}(t) = \langle \mathcal{R}_c^2(t) \rangle_c^{1/2}, \tag{18}$$

where $\mathcal{R}_c(t)$ is the function for a fixed configuration of the classical particles, and $\langle\ \rangle_c$ indicate an ensemble average over these configurations.

For imaginary time, $0 \leqslant \tau \leqslant \beta\hbar$, the function $\mathcal{R}_c(\tau)$ is obtained from the rms distance between beads,

$$\mathcal{R}_c^2(j\beta\hbar/P) = \left\langle \frac{1}{P} \sum_{k=1}^{P} |\mathbf{r}_k - \mathbf{r}_{j+k}|^2 \right\rangle, \tag{19}$$

where $\mathbf{r}_k$ is the position of the k th bead, and here the angular brackets indicate an ensemble average over necklace configurations (electron paths, see Sec. II).

For a free electron the correlation function is given by[15]

$$\mathcal{R}_{\text{free}}(\tau) = \sqrt{3}\lambda_T [(\tau/\beta\hbar)(1 - \tau/\beta\hbar)]^{1/2}, \tag{20}$$

where $\lambda_T = \hbar(\beta/m_e)^{1/2}$ is the electron thermal wavelength. It is instructive to examine the values of $\mathcal{R}(\tau)$ for $\tau = \beta\hbar/P$ and $\tau = \beta\hbar/2$, and the values of the radius of gyration, R_g [see Eq. (7)], of the bead distribution. In Table VI we give the simulation results for $\mathcal{R}(\beta\hbar/2)$, $\sqrt{2}R_g$, and $\sqrt{P}\,\mathcal{R}(\beta\hbar/P)$; each of these quantities is equal to $\mathcal{R}_f \equiv \sqrt{3}\lambda_T/2$ for a free particle. We see that $\mathcal{R}(\beta\hbar/2)$ and R_g, which are measures of the size of the electron distribution, are much smaller than the free particle values indicating

TABLE VI. Values of the complex time correlation function $\mathscr{R}(\tau)$ for $\tau = \frac{1}{2}(\beta\hbar)$ and $\beta\hbar/P$ and for the radius of gyration R_g, for $(H_2O)_n^-$ clusters, at several temperatures. Surface and internal localization states are denoted by (SS) and (IS), respectively. The results for the $(H_2O)_8^-$ cluster in the static configuration used in the quantum-chemical calculations and employed in the construction of the electron–water pseudopotential are denoted by an asterisk. At the bottom of the table, values for a free electron are given for reference. Length in unit of Bohr radius, a_0.

n	T(K)	$\mathscr{R}(\beta\hbar/2)$	$\sqrt{2}R_g$	$\sqrt{P}\,\mathscr{R}(\beta\hbar/P)$
2	20	53	51	109.5
8*	79	9.0	9.1	54.0
	158	8.3	8.6	38.0
8 (SS)	79	15.5	15.0	54.5
(SS)	158	13.7	13.2	38.5
12 (SS)	79	8.4	8.5	54.0
(SS)	158	8.5	8.5	38.1
18 (SS)	79	7.8	7.8	53.5
(SS)	300	6.4	6.5	27.6
(IS)	79	5.8	5.8	53.5
(IS)	158	5.5	5.6	37.7
32 (SS)	79	9.3	9.1	54.0
(SS)	300	8.4	8.3	27.7
(IS)	79	5.6	5.7	53.0
(IS)	158	5.6	5.5	37.5
64 (SS)	300	7.2	7.3	27.6
(SS)	300	5.4	5.4	27.2
128 (IS)	300	5.6	5.5	27.3
free	20	109.5	109.5	109.5
free	79	54.7	54.7	54.7
free	158	38.7	38.7	38.7
free	300	28.1	28.1	28.1

electron localization. These correlation lengths [$\mathscr{R}(\beta\hbar/2)$] are smaller for the interior states than for the surface states, and are nearly independent of cluster size and temperature for the interior states. For the surface states the size of the electron distribution decreases as the cluster size increases and the electron becomes more bound.

The imaginary-time correlation function $\mathscr{R}(\tau)$ can be expressed in terms of R_g and the vectors connecting the beads to the barycenter of the electron distribution ($\mathbf{r}_{\rm ebc}$):

$$\mathscr{R}^2(\tau) = 2R_g^2 - 2\langle[\mathbf{r}(t) - \mathbf{r}_{\rm ebc}]\cdot[\mathbf{r}(t+\tau) - \mathbf{r}_{\rm ebc}]\rangle. \tag{21}$$

The term in brackets equals R_g^2 for $\tau = 0$ or $\beta\hbar$, and decreases as τ approaches $\beta\hbar/2$. For a free particle this term vanishes at $\tau = \beta\hbar/2$, but would clearly be negative for a finite number of beads (take $P = 2$ as a trivial example), leading to the result $\mathscr{R}(\beta\hbar/2) > \sqrt{2}R_g$ if the number of beads is too small. Our results show that, to within the combined statistical uncertainty of about $0.250\,a_0$, the equality $\mathscr{R}(\beta\hbar/2) = \sqrt{2}R_g$ is satisfied.

The correlation between adjacent beads, $\mathscr{R}^2(\beta\hbar/P)$ [see also Eq. (21)] is proportional to the average value of the harmonic potential energy stored in the springs connecting the beads [see fourth term on the right-hand side of Eq. (1)], which would be $(3/2)k_B T$ for a free particle (independent of P). In the presence of an external potential the difference between $\mathscr{R}^2(\beta\hbar/P)$ and the free particle value of $\sqrt{3}\lambda_T/2\sqrt{P}$ should decrease as P increases since the harmonic spring constant is proportional to P and the external potential at the bead position is divided by P [see Eq. (1)]. Our results show that $0.97 < 2\sqrt{P}\,\mathscr{R}(\beta\hbar/P)/\sqrt{3}\lambda_T < 1$, with the smaller values of the ratio corresponding to the interior states. The ratio for simulations with fewer beads is smaller, e.g., for $P = 256$ at $T = 300$ K the ratio is typically $0.87 < 2\sqrt{P}\,\mathscr{R}(\beta\hbar/P)/\sqrt{3}\lambda_T < 0.90$.

In terms of energy eigenvalues E_n and eigenfunctions ψ_n of the excess electron the imaginary time correlation function is given by[15,27]

$$\mathscr{R}_c^2(\tau) = \mathscr{R}_c^2(\beta\hbar/2) + 2\sum_{n>0} e^{-\epsilon_n} \sum_{m>n} \mathscr{R}_{nm}^{(2)} e^{-\epsilon_{nm}/2} \times\{\cosh[(\tau/\beta\hbar - 1/2)\epsilon_{nm}] - 1\}, \tag{22}$$

where $\epsilon_n = \beta(E_n - E_0)$, $\epsilon_{nm} = \epsilon_m - \epsilon_n$, and $\mathscr{R}_{nm}^{(2)}$ is the matrix element,

$$\mathscr{R}_{nm}^{(2)} = \int d\mathbf{r} \int d\mathbf{r}'\psi_n(\mathbf{r})\psi_m^*(\mathbf{r})|\mathbf{r} - \mathbf{r}'|^2\psi_n^*(\mathbf{r}')\psi_m(\mathbf{r}'), \tag{23}$$

where ψ_n is the wave function. Note that although it is not explicitly indicated, the energies and matrix elements depend on the external potential, i.e., on the configuration of the classical particles. The value at $\tau = \beta\hbar/2$ is given by

$$\mathscr{R}_c^2(\beta\hbar/2) = \sum_{n,m} \mathscr{R}_{nm}^{(2)} e^{-(\epsilon_m + \epsilon_n)/2}. \tag{24}$$

It is possible in principal to use Eqs. (22)–(24) to obtain information about the excited state energies and dipole matrix elements from the simulation results.

Ground state dominance is indicated by a lack of dependence of $\mathscr{R}(\tau)$ on τ for values of τ near the midpoint, $\tau = \beta\hbar/2$. This is indeed the case in all our simulation results. This does not, however, necessarily indicate that only the first excited state contributes to the deviation of $\mathscr{R}(\tau)$ from $\mathscr{R}(\beta\hbar/2)$ (except very near the endpoints). The first excited state may not be bound, in which case the matrix element is small, or there may be situations in which two or more closely spaced states contribute to the sum [see Eqs. (22) and (24)]. If there are no bound excited states the behavior of $\mathscr{R}(\tau)$ may be dominated by resonances in the continuum which have a finite width, and in any case the coupling to the classical degrees of freedom will effectively give every state a finite width even if one assumes that the matrix elements are constant.

In spite of the above mentioned difficulties, we have attempted to fit our results with an equation appropriate for the observed ground state dominance (assuming the energies and matrix elements are independent of the classical particle configurations),

$$\mathscr{R}^2(j\beta\hbar/P) = \mathscr{R}^2(\beta\hbar/2) + \sum_{m=1}^{m_{\max}} \mathscr{R}_{0m}^{(2)} e^{-\epsilon_{0m}} \times\{\cosh[(j/P - 1/2)\epsilon_{0m}] - 1\}. \tag{25}$$

We define $\Delta\mathscr{R}_j^2 = \mathscr{R}^2(j\beta\hbar/P) - \mathscr{R}^2(\beta\hbar/2)$, where $\mathscr{R}^2(\beta\hbar/2)$ is the result of the simulation, and we minimize a function F with respect to $\{\mathscr{R}_{0m}^{(2)}\}$ and $\{\epsilon_{0m}\}$, where F is given by

$$F=\sum_{j=1}^{j_{\max}}\{\ln[\Delta\mathscr{R}_j^2(\text{simulation})/\Delta\mathscr{R}_j^2(\text{fit})]\}^2. \quad (26)$$

Because the statistical uncertainty in $\mathscr{R}^2(j\beta\hbar/P)$ increases for large values of j we take $j_{\max}$ to be small ($\leqslant 0.025\,P$), and we average $\mathscr{R}^2(\tau)$ around the midpoint to get a more accurate value of $\mathscr{R}^2(\beta\hbar/2)$.

From the results of the simulation of $(H_2O)_8^-$ with the molecules fixed in the tetrahedral cage configuration used in the quantum-chemical calculations,[30] we were able to obtain results for two excited states, $\Delta E_1 = E_1 - E_0 \approx 0.024$ hartree and $\Delta E_2 \approx 0.048$ hartree, while a fit using only one excited state gave $\Delta E_1 \approx 0.038$ hartree. In all other cases the attempt to fit with more than one state failed either by resulting in unphysical values of $\mathscr{R}_{0m}^{(2)}$ (i.e., positive), or by exhibiting a strong dependence on $j_{\max}$. The results of fitting with a single excited state are summarized in Table VII. We conclude that there probably are no bound excited states for the smaller cluster sizes (8 and 12 molecules) and that for the larger clusters the lowest excited state is near if not above

TABLE VII. Excitation energies, $\Delta E_1 = E_1 - E_0$ (where $E_0 = -$ EVBE) obtained via fitting of the imaginary time correlation function [see text, Eqs. (25) and (26), for $(H_2O)_n^-$ clusters at several temperatures. Surface and interior states are denoted by (SS) and (IS), respectively. Energy in units of hartree.

n	T(K)	ΔE_1
8*	79	0.038
	158	0.038
8	79	0.012
	158	0.013
12	79	0.037
	158	0.041
18 (SS)	79	0.044
(IS)	79	0.084
32 (SS)	79	0.034
(IS)	79	0.082
(IS)	158	0.083
(IS)	300	0.091
64 (SS)	300	0.051
(IS)	300	0.103
128 (IS)	300	0.092

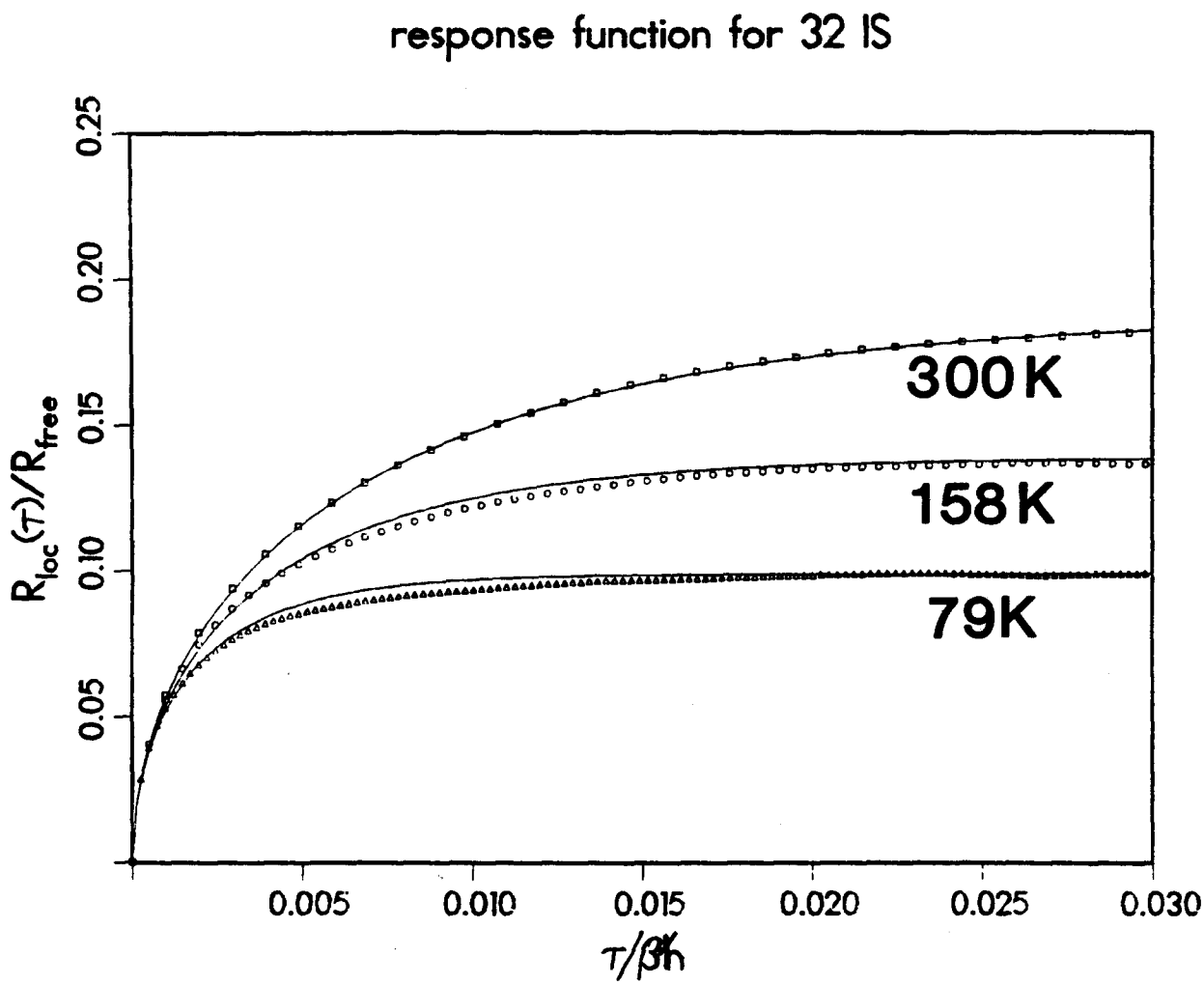

FIG. 15. The imaginary time correlation function $\mathscr{R}(\tau)$, normalized to the free electron value, as a function of $\tau/\beta\hbar$ for small values of the argument, for the internal state of $(H_2O)_{32}^-$ at three temperatures. Data obtained directly from the path-integral simulations are represented by symbols, and the fits to the simulation results [see Eqs. (25) and (26), and Table VII] are given by the solid lines.

continuum limit. Only for the 128 molecule cluster interior state can we conclude unambiguously that there is a bound excited state. The quality of the fits is illustrated in Fig. 14 for the 32 molecule cluster internal states at different temperatures.

In a separate study the electronic energy spectra of $(H_2O)_n^-$ for the interior states of the $n = 32$, 64, and 128 clusters were investigated,[61] using a fast-Fourier transform method for the solution of the Schrödinger equation for the excess electron. In these calculations the nuclear configurations of the water molecules were those obtained via the quantum-path-integral simulations described in this paper and the interaction potential between the excess electron and the water molecules was that given in Eq. (1). The values for ΔE_1 obtained by these calculations are 0.1158, 0.0978, and 0.0875 hartree for the $n = 32$, 64, and 128 clusters, respectively, in approximate agreement with the results given in Table VII. These results which exhibit a trend toward the bulk value (0.0625 hartree = 1.7 eV, at the peak of the excitation band[31]) with increasing cluster size, demonstrate also the effect of long-range interactions on the electronic states of the hydrated electron.

IV. SUMMARY

We have investigated systematically the energetics, stability, structure, and electronic spectra of negatively charged water clusters for a wide range of cluster sizes and at various temperatures. In these studies we have used the quantum-path-integral molecular dynamics method and have employed a newly developed pseudopotential for the description of electron–water interaction. The major result of our studies is the establishment of the modes of localization of an excess electron in water clusters. For medium size clusters $8 \leqslant n \lesssim 32$ the attachment of an electron to the cluster involves the formation of a surface state, while for large clusters an internal localization mode, which can be regarded as the precursor of electron hydration in bulk water, occurs. Our results for the electron binding energies (vertical electron binding energy, EVBE) for the surface states of clusters in the size range $n \leqslant 18$ are in close agreement with the experimental ones obtained via photoelectron spectroscopy.[39] The "transition" from surface to internal excess electron localization mode is manifest by the size dependence of the magnitude of the adiabatic electron binding energy (see Figs. 1 and 2 and Tables II and III) and is exhibited in the range of cluster sizes $n \sim 64$. The energetics of electron attachment to molecular clusters is governed by a balance between the energy of the excess electron interacting with the cluster and the cluster molecular reorganization [E_c, see Eq. (6)] which accompanies the electron localization. While E_c is smaller in magnitude for a surface state than an internal state for all cluster sizes for which the latter is possible ($n = 8$ and 12 do not support an internal state) the gain due to the electron binding dominates in clusters in the size range $n \gtrsim 64$, providing the signature of the onset of a significant contribution from long-range large-polaron attractive interactions for electron localization in large water clusters. Furthermore, we find that even for the largest clusters which we investigated [$(H_2O)_{128}^-$] the bulk limit is not yet achieved, which provides evidence for the importance of long-range interactions in bulk hydration. A decisive determination of the transition between the localization modes may rest on the experimental determination of the vertical electron binding energy from photoelectron spectra, since the predicted values (Figs. 1 and 2 and Tables II and III) are markedly different for the surface and internal modes for clusters in the size range $n \geqslant 32$.

It is of interest to note that in most recent studies[71] we found that for $(NH_3)_n$ clusters the onset of stable electron localization occurs in internal states for $n \geqslant 32$. In contrast to our findings for water, the internal localization in ammonia clusters is not preceded by stable well-bound surface states for smaller clusters. These results are in agreement with the experimentally observed difference between the minimal sizes of clusters of these two polar materials ($n \geqslant 11$ for water[35–41] and $n \geqslant 35$ for ammonia[36,37]) which sustain an excess electron bound state.

ACKNOWLEDGMENTS

This research was supported by the U. S. DOE under Grant No. FG05-86ER45234 (to U. L.) and in part by Grant No. 85-00361 of the US–Israel Binational Science Foundation, Jerusalem (to J. J. and U. L.).

[1]W. Weyl, Ann. Phys. (Leipzig) **197**, 601 (1863).
[2]E. J. Hart and J. W. Boag, J. Am. Chem. Soc. **84**, 4090 (1962).
[3]J. Phys. Chem. **88**, 3699–3913 (1984).
[4]J. Phys. Chem. **84**, 1065–1298 (1980).
[5]J. Phys. Chem. **79**, 2795–3079 (1975).
[6]Ber. Bunsenges. Phys. Chem. **75**, 607–722 (1971).
[7]J. Jortner, J. Chem. Phys. **30**, 839 (1959).
[8]J. Jortner, Rad. Res. Suppl. **4**, 24 (1964).
[9]D. A. Copeland, N. R. Kestner, and J. Kortner, J. Chem. Phys. **53**, 1189 (1970).
[10]J. Jortner, Ber. Bunsenges. Phys. Chem. **75**, 646 (1971).
[11]K. Fueki, D. F. Feng, and L. Kevan, J. Am. Chem. Soc. **95**, 1398 (1973).
[12]N. R. Kestner, in *Electrons in Fluids*, edited by J. Jortner and N. R. Kestner (Springer, Berlin, 1973), p. 1.
[13]M. Newton, J. Chem. Phys. **58**, 5833 (1973).
[14]M. Newton, J. Phys. Chem. **79**, 2795 (1975).
[15]D. Chandler, Y. Singh, and D. M. Richardson, J. Chem. Phys. **81**, 1975 (1984); A. L. Nichols III and D. Chandler, *ibid.* **84**, 398 (1986).
[16]M. Parinello and A. Rahman, J. Chem. Phys. **80**, 860 (1984).
[17]J. Bartholomew, R. Hall, and B. J. Berne, Phys. Rev. B **32**, 548 (1985).
[18]M. Sprik, R. W. Impy, and M. L. Klein, J. Chem. Phys. **83**, 5802 (1985).
[19]B. DeRaedt, M. Sprik, and M. L. Klein, J. Chem. Phys. **80**, 5719 (1984).
[20]M. Sprik, M. L. Klein, and D. Chandler, Phys. Rev. B **32**, 545 (1985).
[21]C. D. Jonah, C. Romero, and A. Rahman, Chem. Phys. Lett. **123**, 209 (1986).
[22]A. Wallqvist, T. Thirumalai, and B. J. Berne, J. Chem. Phys. **85**, 1583 (1986).
[23]A. Wallqvist, D. Thirumalai, and B. J. Berne, J. Chem. Phys. **85**, 6404 (1987).
[24]D. F. Coker, B. J. Berne, and D. Thirumalai, J. Chem. Phys. **86**, 5689 (1987).
[25]P. J. Rossky, J. Schnitker, and R. A. Kuharski, J. Stat. Phys. **43**, 949 (1986).
[26]J. Schnitker and P. J. Rossky, J. Chem. Phys. **86**, 3462 (1987).
[27]J. Schnitker and P. J. Rossky, J. Chem. Phys. **86**, 3471 (1987).
[28]U. Landman, R. N. Barnett, C. L. Cleveland, D. Scharf, and J. Jortner, J. Phys. Chem. **91**, 4890 (1987).
[29]R. N. Barnett, U. Landman, C. L. Cleveland, and J. Jortner, Phys. Rev. Lett. **59**, 811 (1987).
[30]B. R. Rao and N. R. Kestner, J. Chem. Phys. **80**, 1587 (1984).
[31]E. J. Hart and M. Anbar, *The Hydrated Electron* (Wiley, New York, 1970); G. A. Kenney-Wallace, Acc. Chem. Res. **11**, 433 (1978).

[32]R. R. Hents, Farhataziz, and E. M. Hansen, J. Chem. Phys. **55**, 4974 (1972); **57**, 2959 (1974).
[33]L. Kevan, Acc. Chem. Res. **14**, 138 (1981).
[34]D. P. Lin and L. Kevan, J. Phys. Chem. **86**, 2629 (1982).
[35]M. Armbuster, H. Haberland, and H. G. Schindler, Phys. Rev. Lett. **47**, 323 (1981).
[36]H. Haberland, C. Ludewigt, H. G. Schindler, and D. R. Worsnop, Surf. Sci. **156**, 157 (1985).
[37]H. Haberland, H. Langosch, H. G. Schindler, and D. R. Worsnop, Ber. Bunsenges. Phys. Chem. **88**, 270 (1984).
[38]H. Haberland, H. G. Schindler, and D. R. Worsnop, J. Chem. Phys. **81**, 3742 (1984).
[39]J. V. Coe, D. R. Worsnop, and K. H. Bowen, J. Chem. Phys. (to be published).
[40]M. Knapp, O. Echt, D. Kreisle, and E. Recknagel, J. Chem. Phys. **85**, 636 (1986).
[41]M. Knapp, O. Echt, D. Kreisle, and E. Recknagel, J. Phys. Chem. **91**, 2601 (1987).
[42]L. J. de Koning and N. M. H. Nibbering, J. Am. Chem. Soc. **106**, 7971 (1984).
[43]H. J. Werner, V. Manz, and P. Rosmus (unpublished).
[44]K. Eiben and I. Taub, Nature (London) **216**, 782 (1967).
[45]*Solutions Metal–Ammoniac*, edited by G. Lepourte and M. Sienko (Benjamin, New York, 1964).
[46]*Metal–Ammonia Solutions*, edited by J. J. Lagowski and M. Sienko (Butterworths, London, 1970).
[47]*Electrons in Fluids*, edited by J. Jortner and N. R. Kestner (Springer, Berlin, 1973).
[48]*Solvated Electrons*, Advances in Chemistry Series, edited by R. F. Gould (American Chemical Society, Washington, D.C., 1965), Vol. 50.
[49]*Electron-Solvent and Anion-Solvent Interactions*, edited by L. Kevan and B. C. Webster (Elsevier, Amsterdam, 1976).
[50]J. C. Thompson, *Electrons in Liquid Ammonia* (Clarendon, Oxford, 1976).
[51]Can. J. Chem. **55**, 1795–2277 (1977).
[52]A. Gaathon, G. Czapski, and J. Jortner, J. Chem. Phys. **58**, 2648 (1973).
[53]U. Landman, D. Scharf, and J. Jortner, Phys. Rev. Lett. **54**, 1860 (1985).
[54]C. L. Cleveland, U. Landman, R. N. Barnett, and J. Jortner (unpublished).
[55]D. Scharf, J. Jortner, and U. Landman, J. Chem. Phys. (submitted).
[56]J. Jortner, D. Scharf, and U. Landman, in *Elemental and Metallic Clusters*, edited by T. P. Patrick and G. Benedek (Springer, Berlin, 1988).
[57]J. Jortner and A. Gaathon, Can. J. Chem. **55**, 1801 (1977).
[58]P. Krebs, Ber. Bunsenges. Phys. Chem. **88**, 275 (1984).
[59]A. Gaathon, Thesis, Hebrew University, Jerusalem, 1974.
[60]D. J. Chipman, J. Phys. Chem. **82**, 1980 (1978).
[61]R. N. Barnett, U. Landman, and A. Nitzan, Phys. Rev. B (submitted).
[62]N. R. Kestner and J. Jortner, J. Phys. Chem. **88**, 3818 (1989).
[63]R. N. Barnett, U. Landman, C. L. Cleveland, and J. Jortner, J. Chem. Phys. **88**, 4421 (1988).
[64]R. P. Feynman and A. R. Hibbs, *Quantum Mechanics and Path-Integrals* (McGraw-Hill, New York, 1965); R. P. Feynman, *Statistical Mechanics* (Benjamin, Reading, 1972).
[65]D. Chandler and P. G. Wolyness, J. Chem. Phys. **74**, 4078 (1981).
[66]J. R. Fox and H. C. Anderson, J. Phys. Chem. **88**, 4019 (1984).
[67]J. R. Reimers, R. O. Watts, and M. L. Klein, Chem. Phys. **64**, 95 (1982); J. R. Reimers and R. O. Watts, *ibid.* **85**, 83 (1984).
[68]M. F. Herman, E. J. Bruskin, and B. J. Berne, J. Chem. Phys. **76**, 5150 (1982).
[69]R. A. Marcus, J. Chem. Phys. **24**, 979 (1956).
[70]J. Jortner, Mol. Phys. **5**, 257 (1962).
[71]R. N. Barnett, U. Landman, C. L. Cleveland, N. R. Kestner, and J. Jortner, Chem. Phys. Lett. (submitted).